J. Phase Equilib. Diffus. (2026) 47:141–165
https://doi.org/10.1007/s11669-026-01230-w

ORIGINAL RESEARCH ARTICLE

Application of Third-Generation CALPHAD to Elemental Hf, Binary Reassessments and Prediction of the Ternary Hf–Nb–Zr System

Gabriele Traversari[1] · Mariano Casu[1] · Alberto Cincotti[1] · Roberto Orrù[1] · Giacomo Cao[1] · Antonio Mario Locci[1]

Submitted: 18 August 2025 / in revised form: 18 December 2025 / Accepted: 28 January 2026 / Published online: 3 April 2026

Abstract Understanding and predicting the thermodynamic behavior, as well as their mutual interaction, of refractory metal constituents of High-Entropy Borides (HEBs) are essential for designing the compositions of such ceramics with enhanced oxidation-resistant capabilities. In this context, advanced CALPHAD models may provide fundamental thermodynamic descriptions, including the accurate representation of metastable solid and liquid phases, which are crucial for investigating high-temperature oxidation mechanisms and phase stability of HEBs. In this work, the third-generation CALPHAD approach is extended to elemental Hf, incorporating a complete thermodynamic description of its metastable FCC phase, in addition to the stable HCP and BCC structures, and of the liquid phase, including its behavior in the metastable region below the melting point. The Hf–Nb and Hf–Zr binary systems are also re-assessed based on the updated thermodynamic model of Hf. Then, taking advantage of these binary assessments, predictions on the Hf–Nb–Zr ternary phase diagram, for which no prior CALPHAD studies exist, are presented. This investigation represents a step toward the development of a robust, thermodynamics-based tool for modeling oxidation mechanisms and guiding the compositional design of highly resistant HEBs.

Keywords binary · CALPHAD · phase diagram · ternary

✉ Antonio Mario Locci
antoniom.locci@unica.it

[1] Università degli Studi di Cagliari, Dipartimento di Ingegneria Meccanica, Chimica e dei Materiali, Via Marengo, 3 09123 Cagliari, Italy

1 Introduction

High-entropy borides (HEBs), based on the combination of multiple transition metal diborides (HfB_2, ZrB_2, TiB_2, NbB_2, etc.) in near to equimolar proportions, have emerged as a novel class of ultra-high-temperature ceramics, whose thermomechanical properties are not simply given by the average values of their individual constituents.[1-3] Their potential ability to maintain structural integrity and to resist chemical degradation under extreme conditions has positioned them as suitable materials for high-temperature technologies, making them promising candidates for aerospace propulsion systems, nuclear reactors, and thermal protection materials.[4]

Among the critical properties of HEBs, oxidation resistance is particularly important for their performance in such environments. Indeed, oxidation processes can rapidly degrade structural integrity, thus limiting the applicability of these materials where prolonged exposure to high-temperature oxidizing atmospheres is unavoidable.[5,6] Therefore, developing suitable HEB formulations to strategically maximize oxidation resistance is essential. This compositional design requires a fundamental understanding of the thermodynamic stability of refractory metals and their oxides, as well as the interactions among constituent elements at high temperatures.

During oxidation, complex mechanisms involving the formation of individual and mixed oxides as well as transient liquid phases are frequently observed.[7-9] In particular, the formation of liquid boron oxide (B_2O_3), which dissolves refractory metal species, plays a crucial role in oxidation behavior.[10,11] This process occurs at temperatures significantly below the melting points of refractory metals, underscoring the importance of accurately describing liquid metal thermodynamics in

metastable regimes. Thus, a rigorous thermodynamic description of interactions among HEB metal constituents is a prerequisite for elucidating oxidation mechanisms and enabling predictive modeling of phase stability under non-equilibrium conditions.

The CALPHAD (CALculation of PHAse Diagrams) method provides a robust framework for predicting phase equilibria and thermodynamic properties in multi-component systems.[12] In particular, third-generation CALPHAD models incorporate a more physical description of metastable states that, in turn, may enable a refined representation of molten phases.[13] This approach has already been successfully applied to describe several elements and to reassess the corresponding binary phase diagrams,[14-27] providing improved predictive capability for complex alloy systems.[28-30] Extending this methodology to model Hf and its interactions with Nb and Zr is therefore crucial for establishing a comprehensive thermodynamic foundation and, in turn, for the design of HEBs involving these refractory metals as well as for modeling their oxidation behavior.

As far as elemental Hf is concerned, third-generation CALPHAD models have so far been applied only to describe the stable solid HCP and BCC phases,[31,32] while a complete thermodynamic description of the metastable FCC and the liquid phases is still lacking. In this work, the third-generation CALPHAD approach to elemental Hf is addressed providing a comprehensive thermodynamic model that includes both metastable solid and liquid phases. Furthermore, the Hf–Nb and Hf–Zr binary systems are re-assessed, leveraging the updated thermodynamic models of Nb and Zr from our previous study.[23] Notably, at the best of authors' knowledge, only one experimental investigation of the Hf–Nb–Zr ternary phase diagram is available so far in the literature,[33] and no CALPHAD-based assessments or predictions have been reported to date for this system. Therefore, this study also presents predictions on the Hf–Nb–Zr ternary phase diagram, as well as the comparison with the published experimental data. Particular attention is devoted to the stability of the BCC A2 solid solution and the behavior of the liquid phase, providing a valuable basis for future studies on the oxidation mechanisms and compositional design of HEBs.

2 Literature Review of Experimental and Assessed Data

2.1 Pure Hf

Experimental information of elemental hafnium has been collected and reviewed by Arblaster[34] and Paulson et al.[35] The selected data for the condensed phases used in this work are reported in Table 1. Please note that data for the liquid phase taken from Paradis et al.[52] are adjusted in this work by using the estimated value of the emissivity of the solid phase at the melting temperature, instead of the value reported by the authors (see next). The data reported by Arblaster[34] for the gas phase were also adopted in this work.

2.2 The Hf-Nb System

To the best of authors' knowledge, there are only two assessments available for this system.[55,56] Using the same thermodynamic description of the unary endmembers, as well as the same experimental data, these authors calculated the interaction parameters and obtained comparable results. Both assessments do not show the formation of any stable compound and describe the thermodynamic properties of elements according to the second-generation CALPHAD database.[57] In the present work, Fernández Guillermet's assessment[55] is taken into account for the comparison with the binary phase diagram resulting from the proposed third generation-based approach.

2.3 The Hf-Zr System

Only two assessments are available for this system.[58,59] However, only the work of Bittermann and Rogl[59] describes the thermodynamic properties of elements by using the CALPHAD method. In the present work, Bittermann and Rogl's assessment[59] is then considered for the comparison with the binary phase diagram resulting from the proposed third generation-based thermodynamic description. It is worth noting that no stable compounds have been reported so far in Hf-Zr CALPHAD assessments, although some reports mentioned the existence of the intermetallic compound $HfZr_2$.[60,61] In addition, thermodynamic stability of this intermetallic has been assessed at 0 K through ab initio calculations.[62–65] Therefore, this intermetallic phase is included in the proposed thermodynamic description and the formation energy (−25 meV/atom relative to pure Hf and Zr) reported in the Open Quantum Materials Database (OQMD)[63,64] is used in this work for the prediction of its thermodynamic stability.

2.4 The Hf-Nb-Zr System

Experimental findings related to Hf-Nb-Zr ternary solid solutions have been reported by Fedorov et al.[33] These authors investigated the phase formation by *x*-rays analysis of samples obtained by annealing at 1000 and 1700 °C followed by quenching. Electron-irradiation-induced structural changes in Hf-Nb-Zr alloys have been

Table 1 Experimental data selected from scientific literature for the condensed phases of Hf

Phase	Heat capacity	Enthalpy
HCP A3	Adenstedt[36];Wolcott[37];Burk et al.[38];Kneip et al.[39];McClaine[40];Collings and Ho[41];Filippov and Yurchak[42];Peletskii and Druzhinin[43];Arutyunov et al.[44];Cezairlilyan and McClure[45];Milošević and Maglić[46]	Fieldhouse and Lang[47];Hawkins et al.[48];Golutvin and Maslennikova[49];Kats[50];Cagran et al.[51]
BCC A2	Cezairliyan and McClure[45];Paradis et al.[52]	Kats[50];Rösner-Kuhn et al.[53];Cagran et al.[51]
Liquid	Paradis et al.*[52];Korobenko et al.[54]	Rösner-Kuhn et al.[53];Cagran et al.[51]

*Data adjusted by using corrected emissivity value for the liquid phase (see text).

investigated by Nagase and co-workers.[66,67] To the best of authors' knowledge, the CALPHAD thermodynamic description of the ternary system Hf-Nb-Zr has not yet been reported in literature.

3 Thermodynamic Model

The same third-generation CALPHAD modeling framework adopted by the authors in a recent study[23] has been employed to describe the thermodynamics of pure Hf across its solid (stable, metastable, and amorphous), liquid, and gaseous states. For brevity, the model equations numbered (1) through (20) are summarized in Table 2. The molar Gibbs energy of solid, liquid, and gaseous solutions can be obtained by using the equations from (21) to (25) reported in Table 3.

Thermodynamic properties of the intermetallic phase $HfZr_2$ are estimated through the Neumann-Kopp rule.[68,69] Thus, for a binary compound A_aB_b, heat capacity at constant pressure can be expressed as:

$$C_p^{A_aB_b} = nC_p^{A_{x_A}B_{x_B}} = n\left(x_A C_{p,A}^{\alpha} + x_B C_{p,B}^{\alpha}\right) = aC_{p,A}^{\alpha} + bC_{p,B}^{\alpha} \quad \text{(Eq 26)}$$

where, n is the number of atoms forming the compound, while x_A and x_B are the molar (atomic) fractions of the two components, A and B, respectively.

Accordingly, the other thermodynamic properties, such as enthalpy, entropy and Gibbs energy are calculated as follows:

$$H^{A_aB_b} = nH^{A_{x_A}B_{x_B}} = \Delta E_0^{A_aB_b} + aH_A^{\alpha} + bH_B^{\alpha} \quad \text{(Eq 27)}$$

$$S^{A_aB_b} = nS^{A_{x_A}B_{x_B}} = aS_A^{\alpha} + bS_B^{\alpha} \quad \text{(Eq 28)}$$

$${}^0G^{A_aB_b} = n^0G^{A_{x_A}B_{x_B}} = \Delta E_0^{A_aB_b} + a^0G_A^{\alpha} + b^0G_B^{\alpha} \quad \text{(Eq 29)}$$

where $\Delta E_0^{A_aB_b}$ is the difference between the enthalpy of formation of the stoichiometric compound in J/mol per formula unit and the enthalpy of formation of stable pure components at 0 K. It is worth noting that in Eq 29, the linearly dependent temperature term, which is usually reported in literature, is not considered in this work.[68,69] Indeed, the linearly dependent temperature entropy term in third-generation models disappears but its contribution is incorporated into the GEIN function through θ_E (cf. Table 2).

The basic features of the stepwise procedure used for estimating and optimizing the model parameters are the same as reported in our previous work related to the third-generation CALPHAD description of elemental niobium and zirconium.[23] For brevity, the values obtained for Nb and Zr are therefore not included in this paper. Only primary experimental enthalpy and heat-capacity data were included in the optimization for elemental Hf. Parameter fitting was carried out using non-linear regression techniques implemented in custom Fortran codes, leveraging IMSL numerical libraries. Phase diagrams (binary and ternary) were computed using PANDAT Education 2025,[70] which also facilitated the optimization of solution phase interaction parameters through model equations implemented in a manually composed TDB file, available as Supplementary Material. Multi-component systems are described using the Muggianu's geometric model (cf Eq 24). Experimental data on heat capacity, enthalpy, melting point, and boiling point were used to optimize the thermodynamic parameters.

In principle, the Einstein temperature of the various phases can either be evaluated using theoretical approaches or optimized, depending on the availability of literature estimated data and/or experimentally measured thermodynamic properties. In particular, for hafnium solid phases other than the standard reference stable phase (α) one (HCP A3), the method proposed by Dinsdale et al.[16] can be used. Specifically, the difference in molar entropy between a metastable phase ϕ and the reference stable phase α, $\Delta S^{\alpha\rightarrow\phi}$, is expressed as a function of the ratio between the Einstein temperatures of the two phases:

Table 2 Summary of the third generation CALPHAD model equations for pure elements[23]

Solid state (stable and meta-stable phases)

$$C_p^{\phi} = 3R\left(\frac{\theta_E^{\phi}}{T}\right)^2 \exp\left(\frac{\theta_E^{\phi}}{T}\right)\left[\exp\left(\frac{\theta_E^{\phi}}{T}\right)-1\right]^{-2} + a^{\phi}T + b^{\phi}T^2 + c^{\phi}T^3 \quad (1)$$

$$H^{\phi} = E_0^{\phi} + \tfrac{3}{2}R\theta_E^{\phi}\left[\exp\left(\frac{\theta_E^{\phi}}{T}\right)+1\right]\left[\exp\left(\frac{\theta_E^{\phi}}{T}\right)-1\right]^{-1} + \frac{a^{\phi}}{2}T^2 + \frac{b^{\phi}}{3}T^3 + \frac{c^{\phi}}{4}T^4 \quad (2)$$

$$S^{\phi} = 3R\left\{\frac{\theta_E^{\phi}}{T}\left[\exp\left(\frac{\theta_E^{\phi}}{T}\right)-1\right]^{-1} - \ln\left[1-\exp\left(-\frac{\theta_E^{\phi}}{T}\right)\right]\right\} + a^{\phi}T + \frac{b^{\phi}}{2}T^2 + \frac{c^{\phi}}{3}T^3 \quad (3)$$

$$G^{\phi} = E_0^{\phi} + \tfrac{3}{2}R\theta_E^{\phi} + 3RT\ln\left[1-\exp\left(-\frac{\theta_E^{\phi}}{T}\right)\right] - \frac{a^{\phi}}{2}T^2 - \frac{b^{\phi}}{6}T^3 - \frac{c^{\phi}}{12}T^4 \quad (4)$$

$$H_{\mathrm{SER}}^{\alpha} = E_0^{\alpha} + \tfrac{3}{2}R\theta_E^{\alpha}\left[\exp\left(\frac{\theta_E^{\alpha}}{T_{\mathrm{SER}}}\right)+1\right]\left[\exp\left(\frac{\theta_E^{\alpha}}{T_{\mathrm{SER}}}\right)-1\right]^{-1} + \frac{a^{\alpha}}{2}T_{\mathrm{SER}}^2 + \frac{b^{\alpha}}{3}T_{\mathrm{SER}}^3 + \frac{c^{\alpha}}{4}T_{\mathrm{SER}}^4 \quad (5)$$

$${}^0G^{\phi} = G^{\phi} - H_{\mathrm{SER}}^{\alpha} = \left(E_0^{\phi} - E_0^{\alpha}\right) + Z_{\mathrm{SER}}^{\alpha} + \mathrm{GEIN}\left(\theta_E^{\phi}, T\right) - P^{\phi}(T) \quad (6)$$

$$Z_{\mathrm{SER}}^{\alpha} = -\tfrac{3}{2}R\theta_E^{\alpha}\left[\exp\left(\frac{\theta_E^{\alpha}}{T_{\mathrm{SER}}}\right)+1\right]\left[\exp\left(\frac{\theta_E^{\alpha}}{T_{\mathrm{SER}}}\right)-1\right]^{-1} - \frac{a^{\alpha}}{2}T_{\mathrm{SER}}^2 - \frac{b^{\alpha}}{3}T_{\mathrm{SER}}^3 - \frac{c^{\alpha}}{4}T_{\mathrm{SER}}^4 \quad (7)$$

$$\mathrm{GEIN}\left(\theta_E^{\phi}, T\right) = \tfrac{3}{2}R\theta_E^{\phi} + 3RT\ln\left[1-\exp\left(-\frac{\theta_E^{\phi}}{T}\right)\right] \quad (8)$$

$$P^{\phi}(T) = \frac{a^{\phi}}{2}T^2 + \frac{b^{\phi}}{6}T^3 + \frac{b^{\phi}}{12}T^4 \quad (9)$$

Amorphous and liquid state phases

$$C_p^{\mathrm{liq-am}} = C_p^{\mathrm{am}} - C\xi_{\mathrm{eq}} + \left(A^{\mathrm{liq}} - C^{\mathrm{liq}}T\right)\frac{d\xi_{\mathrm{eq}}}{dT} \quad (10)$$

$$\Delta G^{\mathrm{liq-am}} = A^{\mathrm{liq}} - B^{\mathrm{liq}}T + C^{\mathrm{liq}}T\ln T \quad (11)$$

$$G^{\mathrm{liq-am}} = G^{\mathrm{am}} + \xi\Delta G^{\mathrm{liq-am}} + RT[(1-\xi)\ln(1-\xi) + \xi\ln(\xi)] \quad (12)$$

$$\xi_{\mathrm{eq}} = \left[1+\exp\left(\frac{\Delta G^{\mathrm{liq-am}}}{RT}\right)\right]^{-1} \quad (13)$$

$$\frac{\mathrm{d}\xi_{\mathrm{eq}}}{\mathrm{d}T} = \frac{\left(A^{\mathrm{liq}} - C^{\mathrm{liq}}T\right)}{RT^2}\left(\xi_{\mathrm{eq}} - \xi_{\mathrm{eq}}^2\right) \quad (14)$$

$$H^{\mathrm{liq-am}} = H^{\mathrm{am}} + \xi_{eq}\left(A^{\mathrm{liq}} - C^{\mathrm{liq}}T\right) \quad (15)$$

$$S^{\mathrm{liq-am}} = S^{\mathrm{am}} - \xi_{\mathrm{eq}}\left[-B^{\mathrm{liq}} + C^{\mathrm{liq}}(1+\ln T)\right] - \tfrac{1}{T}\mathrm{G2ST}\left(\Delta G^{\mathrm{liq-am}}\right) \quad (16)$$

$$G^{\mathrm{liq-am}} = G^{\mathrm{am}} + \mathrm{G2ST}\left(\Delta G^{\mathrm{liq-am}}\right) \quad (17)$$

$$\mathrm{G2ST}\left(\Delta G^{\mathrm{liq-am}}\right) = -RT\ln\left[1+\exp\left(-\frac{\Delta G^{\mathrm{liq-am}}}{RT}\right)\right] \quad (18)$$

$${}^0G^{\mathrm{liq-am}} = \left(E_0^{\mathrm{am}} - E_0^{\alpha}\right) + Z_{\mathrm{SER}}^{\alpha} + \mathrm{GEIN}\left(\theta_E^{\mathrm{am}}, T\right) - P^{\mathrm{am}}(T) + \mathrm{G2ST}\left(\Delta G^{\mathrm{liq-am}}\right) \quad (19)$$

Gas phase

$${}^0G^{\mathrm{gas}} = a_0^{\mathrm{gas}} + a_1^{\mathrm{gas}}\mathrm{T}\ln T + \sum_{i=1}^{10} a_{i+1}^{\mathrm{gas}}T^i \quad (20)$$

T_{SER} = 298.15 K and P_{SER} = 10^5 Pa

$$\Delta S^{\alpha\to\phi} = 3R\ln\left(\frac{\theta_E^{\phi}}{\theta_E^{\alpha}}\right) \quad \text{(Eq 30)}$$

Therefore, if $\Delta S^{\alpha\to\phi}$ is known, the Einstein temperature of the metastable phase can be calculated by using the following relation:

$$\theta_E^{\phi} = \theta_E^{\alpha}\exp\left(-\frac{\Delta S^{\alpha\to\phi}}{3R}\right) \quad \text{(Eq 31)}$$

Moreover, for the specific case of hafnium, the Einstein temperatures of all solid phases can also be evaluated based on the Debye temperatures reported by Chen and Sundman.[71] In this work, the Einstein temperature of each phase was then determined, wherever possible, by both optimization and Dinsdale's method[16] (cf. Eq 31), and the results were compared with the theoretical estimations provided by Chen and Sundman in the aforementioned study.[71]

The hexagonal crystal structure of Hf is stable from 0 K to 2016 K[34]; then the phase transition to the BCC A2 structure occurs. The difference $E_{0,Hf}^{BCC\,A2} - E_{0,Hf}^{HCP\,A3}$, which is required to calculate ${}^0G_{Hf}^{BCC\,A2}$ (cf. Eq 6), was also treated as an adjustable parameter during the optimization procedure. In fact, the corresponding value reported in the Open Quantum Materials Database (OQMD)[63,64] was not adopted in this work, since when using such energy difference, the model is able to reproduce the heat capacity but failed to accurately predict the enthalpy. Heat capacity

Table 3 Model equations for solution phases

Solution phases	
${}^{0}G_{\text{mix}}^{\phi} = {}^{\text{REF}}G_{\text{mix}}^{\phi} + {}^{\text{ID}}G_{\text{mix}}^{\phi} + {}^{\text{EX}}G_{\text{mix}}^{\phi}$	(21)
${}^{\text{REF}}G_{\text{mix}}^{\phi} = \sum_{i=1}^{n} x_i^{\phi}\,{}^{0}G_i^{\phi}$	(22)
${}^{\text{ID}}G_{\text{mix}}^{\phi} = RT\sum_{i=1}^{n} x_i^{\phi}\ln x_i^{\phi}$	(23)
${}^{\text{EX}}G_{\text{mix}}^{\phi} = {}^{\text{EX}}G_{\text{mix,bin}}^{\phi} = \sum_{i=1}^{n-1}\sum_{j>i}^{n} x_i^{\phi}x_j^{\phi}\sum_{k=0}^{l^{\phi}} {}^{k}L_{i,j:\text{Va}}^{\phi}\left(x_i^{\phi}-x_j^{\phi}\right)^{k}$	(24)
${}^{k}L_{i,j:\text{Va}}^{\phi} = {}^{k}a_{i,j:\text{Va}}^{\phi} + {}^{k}b_{i,j:\text{Va}}^{\phi}T$	(25)

and enthalpy experimental data of BCC A2 were fitted by imposing the constraint ${}^{0}G_{\text{Hf}}^{\text{BCC A2}} = {}^{0}G_{\text{Hf}}^{\text{HCP A3}}$ at the transition temperature. In the case of FCC phase, no experimental data are available; therefore, optimization could not be performed. The Einstein temperature of this phase was instead estimated using the two alternative approaches previously applied to the BCC phase. The coefficients of the polynomial were set equal to those of the HCP phase, following the standard procedure used in the context of the third-generation description. Finally, the method proposed by He et al.[13] was adopted in this work to prevent the re-stabilization of solid phases at high temperatures (see Supplementary material for details).

Thermodynamic properties of liquid Hf are assessed using the two-state model for liquid-amorphous phases.[72,73] The number of adjustable parameters is reduced as much as possible, due to the lack of experimental data available for the liquid phase below the melting temperature. As presented in our previous work,[23] coefficient a^{am} should be set equal to the value of the electronic heat capacity of Hf at high temperature, since it is assumed that the electronic heat capacity of liquid-amorphous phase is close to that of the solid at the melting point.[74,75] However, based on author knowledge, no electronic heat capacity for Hf at high temperatures is reported in the literature. Thus, this value is obtained by multiplying the electronic heat capacity of Hf at low temperatures[34] by the ratio between electronic heat capacity at high and low temperatures calculated for Nb, assuming that this ratio is the same for Hf, Nb and Zr.[23]

Experimental data for the heat capacity of liquid Hf are available near the melting point as well as at high temperatures; therefore, the parameter b^{am} was treated as adjustable. The parameter B^{liq} in Eq 12 was fixed to the communal entropy R,[23,76] while A^{liq}, C^{liq}, and the cohesive energy difference $E_0^{\text{am}} - E_0^{\alpha}$ were optimized. It is important to note that, since $\left(\xi_{eq} - \xi_{eq}^2\right) > 0$ in Eq 14, the parameter C^{liq} must be negative to ensure a positive derivative as $T \to \infty$. Heat capacity and enthalpy data were used for parameter optimization, with the additional constraint that ${}^{0}G^{\text{liq-am}} = {}^{0}G^{\text{BCC A2}}$ at the melting temperature of Hf.

It is commonly reported that the emissivity, ε, of the liquid phase can be assumed constant and equal to that of the solid phase at the melting temperature.[77,78] Accordingly, in the case of liquid Hf, heat capacity data from Paradis et al.[52] were corrected using a more accurate emissivity value at the melting point (0.33462), as determined in this work based on measurements for the solid phase carried out by the same authors.[52] Notably, the emissivity value used by these authors for liquid Hf (0.25) is identical to that reported for liquid Nb in their earlier study.[79] Instead, the emissivity value calculated in this work is in good agreement with that one estimated using the following relation from Onufriev et al.[80]:

$$\varepsilon = 2.17810^{-1} + 5.4710^{-5}T \qquad \text{(Eq 32)}$$

As in our previous work,[23] coefficients a_i^{gas} appearing in Eq 20 were obtained by fitting gas phase literature data.[34] Lastly, in order to predict the thermodynamic stability of the stoichiometric compound $HfZr_2$, the value of $\Delta E_0^{HfZr_2} = -7236.88$ J/mol has been calculated starting from the formation energy (−25 meV/atom) reported by OQMD.[63,64]

4 Results and Discussion

This section presents the results of the third-generation CALPHAD modeling, which are organized to reflect the progressive construction of the thermodynamic description from elemental Hf to its binary and ternary systems. First, the thermodynamic description of elemental Hf is developed using the procedure described in Section 3 and the obtained outcomes are compared with both experimental data and previous modeling results. Subsequently, the Hf–Nb and Hf–Zr binary systems are re-assessed using the updated elemental Hf model provided in this work along with the thermodynamic parameters of elemental niobium and zirconium provided in our previous work.[23] Finally, these binary descriptions along with the re-assessed Nb-Zr binary system[23] are combined to predict the Hf–Nb–Zr ternary phase diagram, with emphasis on the stability of the BCC A2 solid solution and the behavior of the liquid phase. No ternary interaction parameters have been estimated due to the lack of reliable experimental data.

Table 4 Thermodynamic model parameters of elemental Hf

phase ϕ	$E_0^\phi - E_0^\alpha$, J mol^{-1}	θ_E^ϕ, K	a^ϕ, J mol^{-1} K^{-2}	b^ϕ, J mol^{-1} K^{-v-1}	c^ϕ, J mol^{-1} K^{-v-1}
FCC A1	6947.4 [(a)]	138.57 [(b)]	3.42879 10^{-3}	2.85023 10^{-6}	-4.88151 10^{-10}
BCC A2	10855.9	111.86	2.45125 10^{-3}	1.07012 10^{-6}	0
HCP A3 (α)	0	149.53	3.42879 10^{-3}	2.85023 10^{-6}	-4.88151 10^{-10}
amorphous	23793	89.17	1.26795 10^{-3} [(c)(d)]	3.99255 10^{-14}	0

phase ϕ	A^{liq}, J mol^{-1}	B^{liq}, J mol^{-1} K^{-1}	C^{liq}, J mol^{-1} K^{-1}
liquid	64167.4	8.31439	− 0.85093

phase ϕ	Parameter	Value
gas	a_0^{gas}	614079.21
	a_1^{gas}	− 24.50304
	a_2^{gas}	− 28.42421
	a_3^{gas}	1.32726 10^{-2}
	a_4^{gas}	− 9.99610 10^{-6}
	a_5^{gas}	3.88428 10^{-9}
	a_6^{gas}	− 8.72211 10^{-13}
	a_7^{gas}	9.51597 10^{-17}
	a_8^{gas}	2.24366 10^{-21}
	a_9^{gas}	− 2.03659 10^{-24}
	a_{10}^{gas}	2.34914 10^{-28}
	a_{11}^{gas}	− 9.45007 10^{-33}

[(a)]Saal et al.[63]; Kirklin et al.[64]; [(b)] Chen and Sundman[71]; [(c)] Arblaster [34]; [(d)] Traversari et al.[23]

4.1 Elemental Hf: Stable and Metastable Phase Descriptions

The model parameters for the thermodynamic description of elemental Hf are summarized in Table 4, and the calculated heat capacities of FCC A1, BCC A2, HCP A3, and liquid Hf are shown in Fig. 1. In particular, the reported values of the Einstein temperature were all obtained through optimization, except for the FCC phase. Parameters a, b, and c were also calculated by fitting the available heat capacity data (see Table 1). However, for the sake of comparison, θ_E was also calculated through Eq 31, wherever possible (e.g. BCC). The corresponding outcomes are reported and compared in Table S.1, along with the estimations obtained using the Debye temperatures provided by Chen and Sundman.[71]

Beginning with the HCP phase, it is worth noting that the fitted value of the Einstein temperature closely matches the estimate obtained using the data reported by Chen and Sundman.[71] Furthermore, the derived thermodynamic description of the HCP phase compares well with literature data in terms of heat capacity (cf. Fig. 1) and the derived molar Gibbs energy (cf. Fig. S.1). Table S.1 also shows that the approaches proposed by Dinsdale et al.[16] and by Chen and Sundman[71] yield notably different estimations for the BCC phase. To interpret this discrepancy, it is important to recall that the first method is based on the assumption of a constant entropy of transition at high temperatures.[16] Figure S.2 shows this quantity as a function of temperature according to the data provided by Dinsdale.[57] It can be clearly seen that $\Delta S^{HCP \rightarrow BCC}$ significantly varies with temperature. Therefore, it seems that the disagreement in the Einstein temperature mentioned above could be ascribed to this peculiar behavior of hafnium, which somehow affects the procedure suggested by Dinsdale et al.[16].

Therefore, in this work, the Einstein temperature of the BCC phase was also treated as a free parameter, and the experimental data were fitted using various forms of the polynomial $P^{BCC}(T)$ (cf. Eq 9). Among the models yielding a high regression coefficient, the one that provided an Einstein temperature closest to the estimation based on Chen and Sundman data (see Table S.1) was selected. Optimization performed with the θ_E of the BCC phase fixed to the exact value calculated through the Chen and

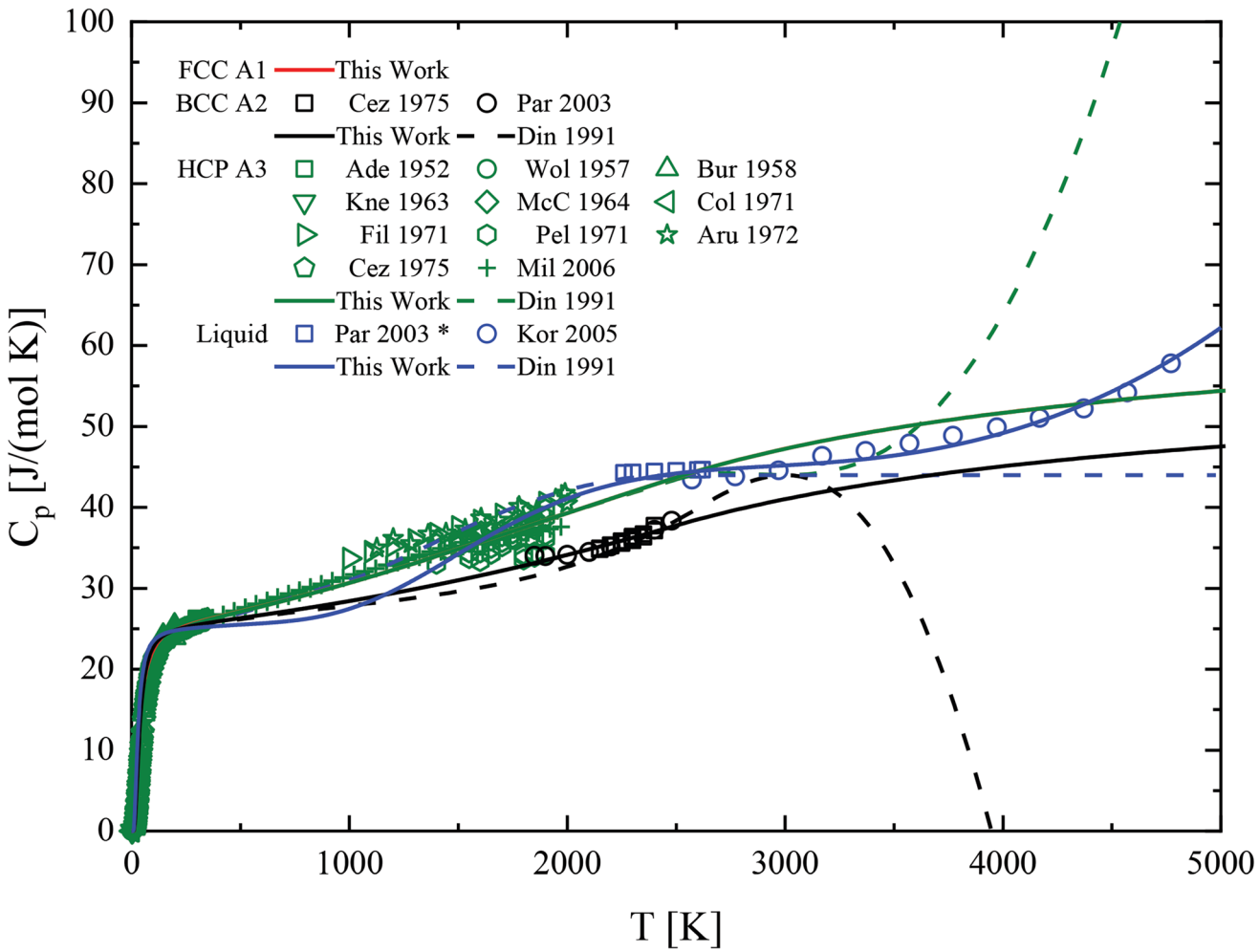

Fig. 1 Calculated temperature profiles of hafnium heat capacity in comparison with experimental data and Dinsdale's model results[57]. Color code should be read as follows: FCC A1 (red), BCC A2 (black), HCP A3 (green), liquid (blue)

Sundman approach[71] resulted in a slightly lower regression coefficient. As previously mentioned in Section 3, no experimental data are available for the metastable FCC phase; therefore, optimization could not be carried out. Regarding θ_E^{FCC}, Table S.1 shows that the approaches based on Dinsdale et al.[16] and Chen and Sundman[71] yield similar estimates. However, to maintain consistency with the case of the BCC phase, where the optimized Einstein temperature was closer to the estimate based on the data of Chen and Sundman[71] than to that from Dinsdale et al.'s method,[16] θ_E^{FCC} was fixed to the value obtained using the former approach.

Different methods were also tested for the liquid/amorphous phase. The corresponding Einstein temperature, along with the other relevant parameters, was first optimized following the procedure described in Section 3. The agreement between the proposed description and the experimental heat capacity data is shown in Fig. 1. The adjusted parameters are reported in Table 4, and the optimized Einstein temperature is also listed in Table S.1. Alternatively, it is worth mentioning that He et al.[13] suggested that $\theta_E^{am/liq}$ can be assumed to be equal to 80% of that of the crystalline phase. However, in the case of elements exhibiting allotropy, such as hafnium, the choice of the reference crystalline phase is not straightforward. Among the elements investigated in the work of He et al., cobalt is the only one that exhibits allotropy. According to Table 5 in their study, $\theta_E^{am/liq}$ for cobalt was estimated to be 80% of the Einstein temperature of its low-temperature stable phase (i.e., HCP). Then this approach was tested for hafnium. Specifically, the optimization was performed by keeping $\theta_E^{am/liq}$ equal to 119.62 K (i.e., = $0.8\theta_E^{HCP}$). The results are shown in Figure S.3 of the Supplementary material, where it can be clearly seen that although the molar enthalpy trend is well reproduced, the agreement with the experimental heat capacity data is not entirely satisfactory.

Table 5 Comparison between the optimized and literature thermodynamic properties of hafnium

Properties	Value	Reference
$C_p^{HCP\,A3}(298.15\ K)$, J mol^{-1} K^{-1}	25.69	Westrum[89]
	25.73	Hultgren *et al.*[90]
	25.72	Spencer[91]
	25.69	Gurvich *et al.*[92]
	25.69	Chase[93]
	25.736	Barin[94]
	25.688	Dinsdale[57]
	25.69	Arblaster[34]
	25.689	This work
$H^{HCP\,A3}(298.15K) - H^{HCP\,A3}(0K)$, J mol^{-1}	5845	Westrum[89]
	5845	Hultgren *et al.*[90]
	5845	Gurvich *et al.*[92]
	5842	Chase[93]
	5845	Arblaster[34]
	5904	This work
$S^{HCP\,A3}(298.15\ K)$, J mol^{-1} K^{-1}	43.56	Westrum[89]
	43.56	Hultgren *et al.*[90]
	43.51	Spencer[91]
	43.56	Gurvich *et al.*[92]
	43.56	Chase[93]
	43.555	Barin[94]
	43.56	Dinsdale[57]
	43.561	Arblaster[34]
	43.561	This work
$C_p^{BCC\,A2}(298.15\ K)$, J mol^{-1} K^{-1}	25.497	Dinsdale[57]
	25.479	This work
$C_p^{BCC\,A2} - C_p^{HCP\,A3}, (T = T_t)$, J mol^{-1} K^{-1}	-1.982	Barin[94]
	-6.599	Dinsdale[57]
	-0.907	Arblaster[34]
	-5.201	This work
$H^{BCC\,A2} - H^{HCP\,A3}, (298.15K)$, J mol^{-1}	12378	Dinsdale[57]
	10729	This work
$H^{BCC\,A2} - H^{HCP\,A3}, (T = T_t)$, J mol^{-1}	5176	Peletskii and Druzhinin[43]
	5200	Martynyuk and Tsapkov[95]
	5908	Cezairlyan and McClure[45]
	3376	Katz[50]
	6736	Barin[94]
	5866	Dinsdale[57]
	5040	Arblaster[34]
	6013	This work
$S^{BCC\,A2}(298.15\ K)$, J mol^{-1} K^{-1}	51.573	Dinsdale[57]
	50.321	This work
$S^{BCC\,A2} - S^{HCP\,A3}, (T = T_t)$, J mol^{-1} K^{-1}	3.346	Barin[94]
	2.921	Dinsdale[57]
	2.500	Arblaster[34]
	2.983	This work
$C_p^{FCC\,A1}(298.15\ K)$, J mol^{-1} K^{-1}	25.688	Dinsdale[57]
	25.762	This work

Table 5 continued

Properties	Value	Reference
$H^{FCC\,A1} - H^{HCP\,A3}, (298.15K)$, J mol^{-1}	10000	Dinsdale[57]
	6925	This work
$S^{FCC\,A1}(298.15)$, J mol^{-1} K^{-1}	45.760	Dinsdale[57]
	45.436	This work
$C_p^{liq}(298.15\,K)$, J mol^{-1} K^{-1}	25.434	Dinsdale[57]
	25.137	This work
$C_p^{liq} - C_p^{BCC\,A2}, (T = T_m)$, J mol^{-1} K^{-1}	-3.347	Barin[94]
	5.556	Dinsdale[57]
	-0.893	Arblaster[34]
	6.435	This work
$H^{liq} - H^{HCP\,A3}, (298.15\,K)$, J mol^{-1}	27402	Dinsdale[57]
	23573	This work
$H^{liq} - H^{BCC\,A2}, (T = T_m)$, J mol^{-1}	25941	Ackermann and Ruth[96]
	24058	Barin[94]
	27196	Dinsdale[57]
	20247	Rösner-Kuhn et al.[53]
	14623	Paradis et al.[52]
	16064	Korobenko et al.[54]
	14690	Cagran et al.[51]
	19855	Arblaster[34]
	18806	This work
$S^{liq}(298.15K)$, J mol^{-1} K^{-1}	54.658	Dinsdale[57]
	55.523	This work
$S^{liq} - S^{BCC\,A2}, (T = T_m)$, J mol^{-1} K^{-1}	9.623	Barin[94]
	10.852	Dinsdale[57]
	7.948	Arblaster[34]
	4.810	This work

It is worth mentioning that the criterion mentioned above was first introduced by Chen and Sundman[72] in their pioneering work on the modeling of the thermodynamic properties of iron according to the third generation of CALPHAD. Specifically, they applied the rule $\theta_E^{am/liq} = 0.8\theta_E^{BCC}$. However, in the case of iron, the BCC structure represents both the low- and high-temperature stable forms, leaving some ambiguity as to which stable form should be considered. Interestingly, when the same relation is applied by considering the high-temperature stable structure of hafnium, we obtain $\theta_E^{am/liq}$ = 89.5 K, which is in very close agreement with the fitted value.

Therefore, among the two approaches considered for the liquid phase, the full optimization method, i.e., including the Einstein temperature as a fitting parameter, was retained since it provides better agreement with the experimental data. At the same time, it appears that the relationship between the Einstein temperature of the liquid/amorphous phase and that of the crystalline phase may deserve further examination, especially for elements exhibiting allotropy, where the choice of the reference crystalline structure may not be univocal.

An overview of the reassessed properties of hafnium and their comparison with reference literature values is provided in Table 5. It should be emphasized that, apart from $S^{HCP\,A3}(298.15\,K)$, all properties reported therein and evaluated in this work represent predictions of the proposed thermodynamic model. Overall, the present results exhibit very good consistency with the most reliable experimental and assessed values reported in the literature, confirming the accuracy of the adopted thermodynamic description. For the low-temperature properties, the optimized values are almost identical to those reported by the various authors. This level of agreement demonstrates that the revised Einstein-based heat-capacity model reproduces the experimental measurements within their uncertainty.

Larger deviations are observed for some of the quantities related to the transition between the α-HCP and β-BCC phases and the latter one to the liquid phase. However, it is

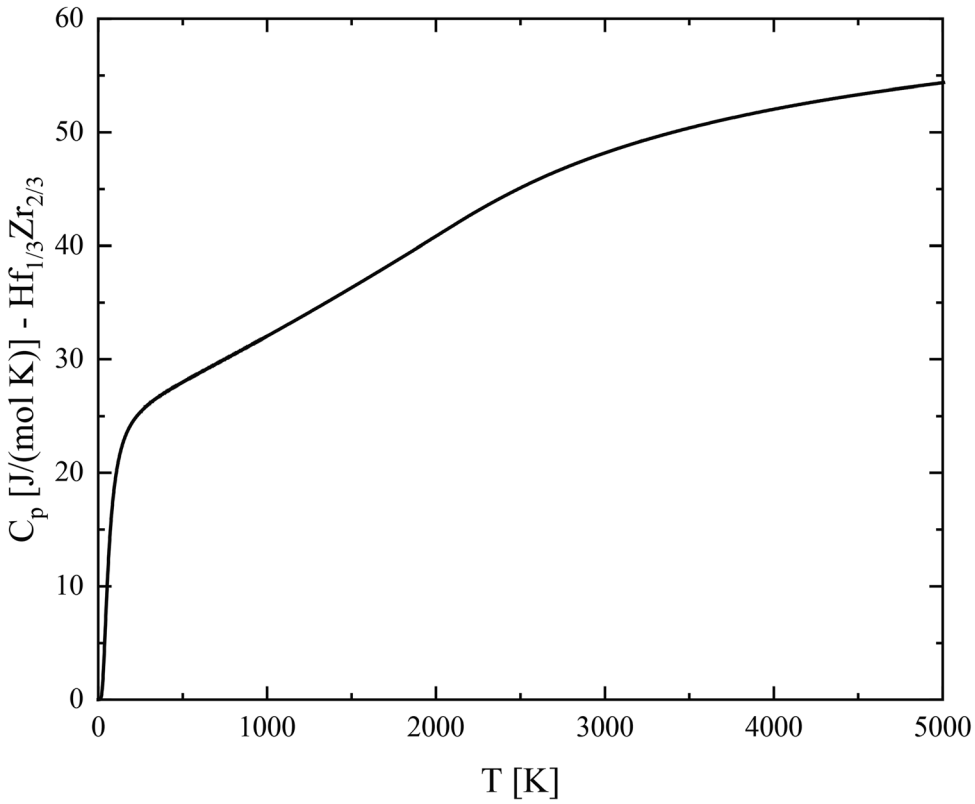

Fig. 2 Calculated heat capacity temperature profile of the stoichiometric compound $HfZr_2$

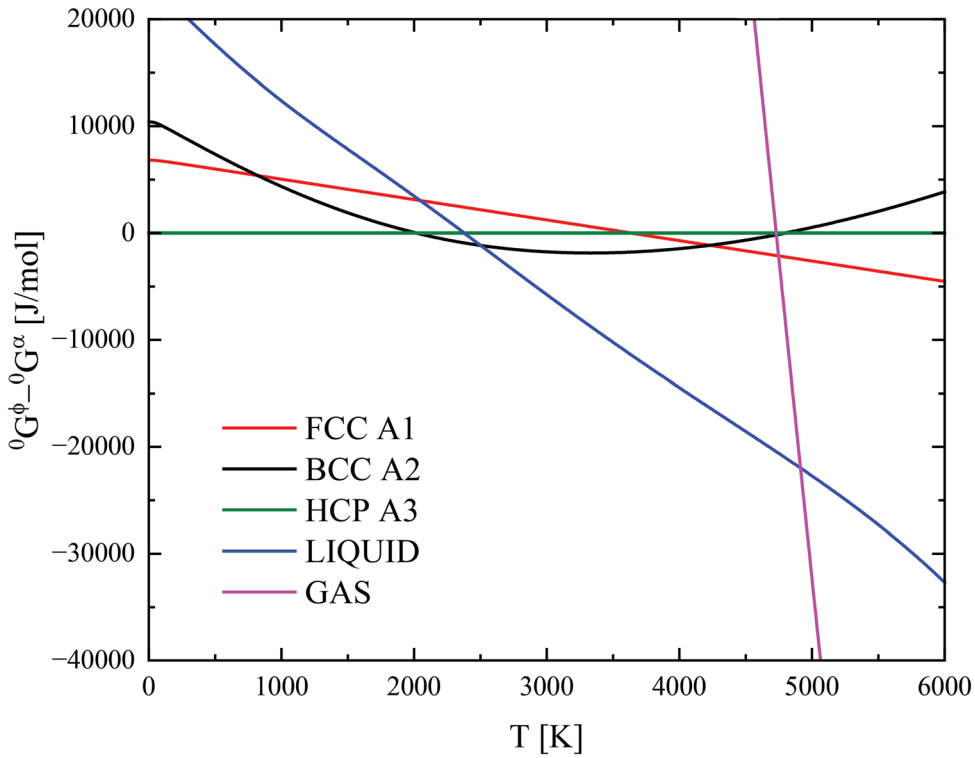

Fig. 3 Calculated molar Gibbs energy temperature profiles of hafnium phases relative to HCP A3

worth noting that, for the properties showing the largest deviations, the corresponding literature data also display the greatest variability among different sources. This indicates that the observed discrepancies are not a consequence of the present optimization procedure but rather reflect the intrinsic scatter and uncertainty of the experimental information available in the literature.

In Figure 1, the calculated heat capacities of FCC A1, BCC A2, HCP A3, and liquid Hf as a function of temperature are compared with the second-generation CALPHAD description by Dinsdale[57] and with the experimental data used for optimization. A very good agreement is observed between the present calculations and experimental data for the HCP and BCC phases. The results are also comparable to those obtained using the Dinsdale's model up to the melting temperature.[57] However, it should be noted that the second-generation description of BCC Hf is expected to be valid only below 3000 K, beyond which the calculated heat capacity of BCC Hf unrealistically, and abnormally, decreases. A notable divergence between the two approaches is also observed for the HCP phase at higher temperatures, with the second-generation model describing a more pronounced increase of the heat capacity as the temperature increases.

No experimental data are available for metastable FCC Hf. As previously discussed for metastable FCC Nb and Zr, and metastable HCP Nb,[23] differences between the FCC Hf phase relative to the stable HCP one are confined to low temperatures, while at higher thermal levels, the heat capacity of FCC Hf converges toward that of the HCP phase. This is expected since the heat capacity coefficients for FCC were constrained to those of HCP (cf. Table 4).

For the liquid phase, the present third-generation model shows very good agreement with experimental data, capturing the temperature-dependent heat capacity from near the melting point to higher temperatures. In contrast, the second-generation model, which assumes a constant heat capacity for the liquid phase above the melting point, fails to reproduce the experimentally observed trend reported by Korobenko et al.[54] Below the melting point, both models are qualitatively similar.

Taking advantage of the third-generation CALPHAD descriptions of elemental Hf (this work) and Zr,[23] the heat capacity of the stoichiometric compound $HfZr_2$ was estimated as described in Section 3. No experimental data for the heat capacity of this compound are available in the literature. As shown in Fig. 2, the calculated temperature dependence of C_p for $HfZr_2$ is given by the molar weighted average of the HCP phases of Hf and Zr, consistent with the modeling assumptions adopted in this work.

Figure 3 presents the relative molar Gibbs energy of all phases of Hf referenced to the stable HCP phase. The results show that the BCC phase is stable only within a narrow temperature range just below the melting point, in agreement with the well-known HCP → BCC transition for Hf.[34] Above this range, the liquid phase becomes stable, and at even higher temperatures, the gas phase dominates. The intersection of the Gibbs energy curves of liquid and gas phases occurs at approximately 4910 K,

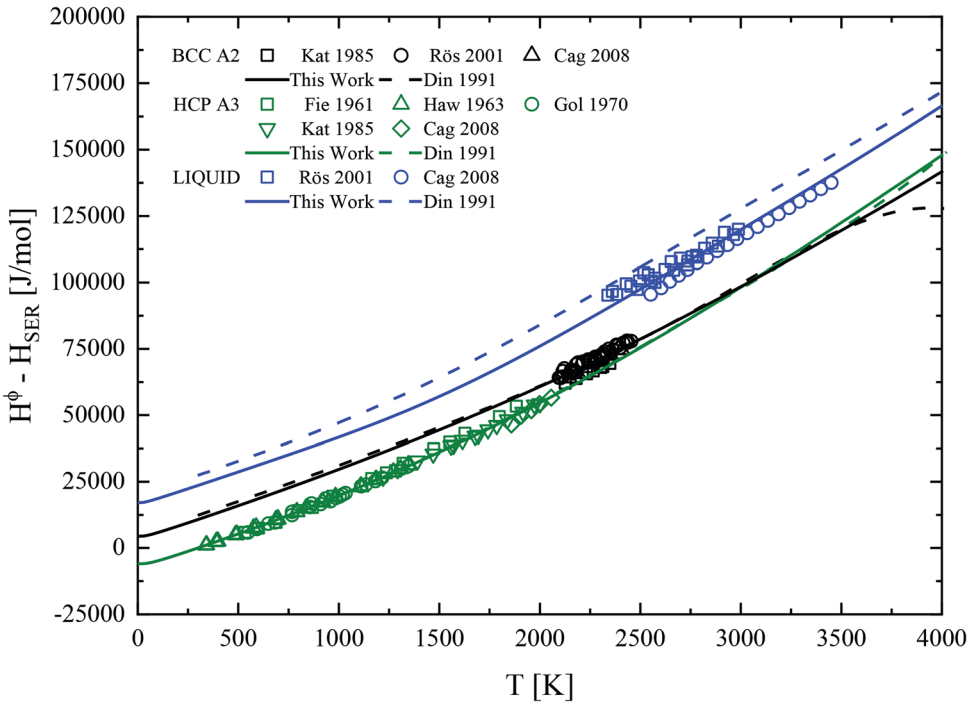

Fig. 4 Calculated temperature profiles of molar enthalpy of solid HCP A3, BCC A2 and liquid hafnium in comparison with experimental data and Dinsdale's model results[57]. Color code should be read as follows: BCC A2 (black), HCP A3 (green), liquid (blue)

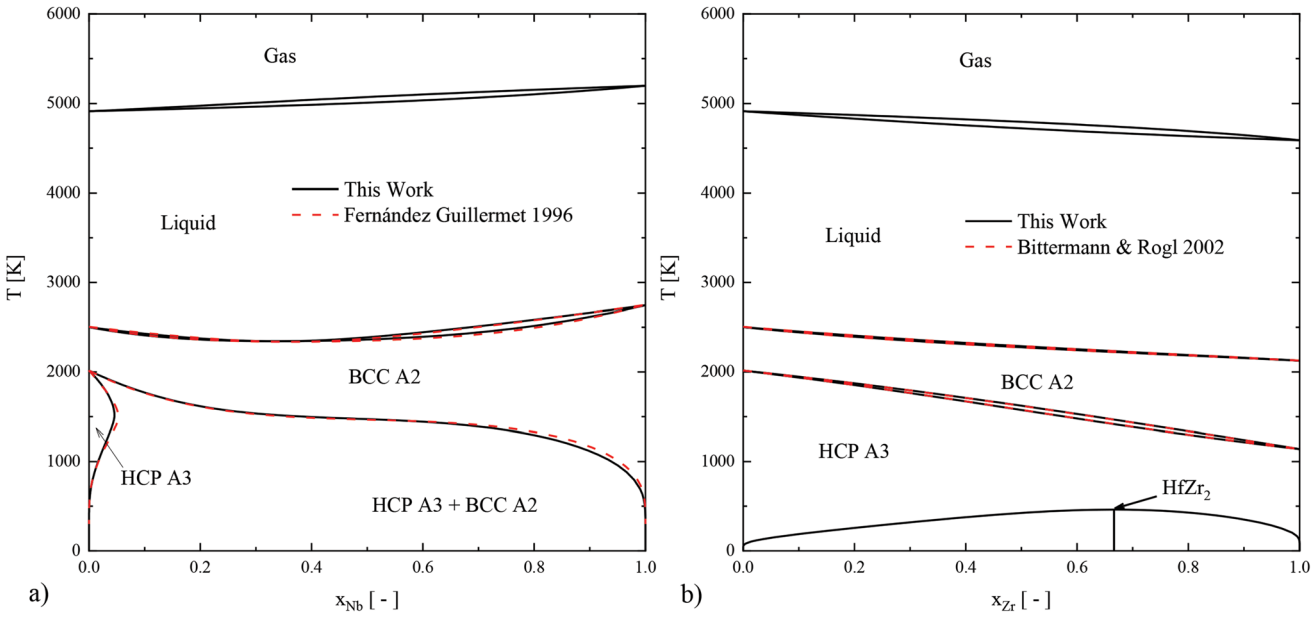

Fig. 5 The phase diagrams calculated using the present thermodynamic description (black line) and the comparison with the previous assessments reported in the literature (dashed red line): (**a**) Hf-Nb; (**b**) Hf-Zr

which is in good agreement with the normal boiling point (NBP) of Hf reported by Arblaster (4850 K).[34] Moreover, these results show that, if the gas phase is suspended, the BCC phase would not re-stabilize at higher temperature because of the adoption of the He et al. method.[13]

A comparison between the calculated molar enthalpy of the HCP, BCC, and liquid phases of Hf and the corresponding experimental data is provided in Fig. 4. The black and blue solid lines represent the fitted results for the BCC and liquid phases, respectively, whose enthalpy data were used to determine the model parameters (see Section 3). The green solid line corresponds to the predicted enthalpy of the HCP phase. The present calculations show excellent agreement with the experimental data available for all phases. The second-generation CALPHAD description of Dinsdale[57] is also plotted for the sake of comparison. While both models agree closely within the temperature ranges where experimental data are available, differences emerge in the metastable regions, specifically, below the melting point for the BCC phase and at high temperatures above the melting point for all the solid phases. It can also be observed that the liquid phase enthalpy calculated in this work is systematically lower than that provided by Dinsdale's description across the investigated range,[57] aligning more closely with the experimental findings and thereby improving the reliability of the metastable liquid phase description. It should be noted that the experimental data used in this work, and reported in Fig. 4, are more recent than those available at the time of Dinsdale's work.[57] This fact may therefore explain the differences observed.

4.2 Reassessment of Hf–Nb and Hf–Zr Binary Systems

The calculated phase diagrams of the two binary systems, Hf-Nb and Hf-Zr, are presented in Fig. 5, while the re-optimized interaction parameters derived in this work are summarized in Table 6 and compared with those reported in earlier assessments. It can be also observed that the coefficients ${}^{k}b^{\phi}_{i,j:\mathrm{Va}}$ (cf. Eq 25) are only non-zero for the HCP and liquid solutions in the Hf-Zr system. According to Dinsdale et al.,[16] the temperature dependence of the excess Gibbs energy of the phase ϕ results from the variation of the Einstein temperature of ϕ with composition quantified by ${}^{k}b^{\phi}_{i,j:\mathrm{Va}}$. Specifically,

$$\ln\theta^{\phi}_{E} = x^{\phi}_{i}\theta^{\phi}_{E,i} + x^{\phi}_{j}\theta^{\phi}_{E,j} + x^{\phi}_{i}x^{\phi}_{j}\ln{}^{0}\theta^{\phi}_{i,j} \qquad \text{(Eq 32)}$$

where

$$\ln{}^{0}\theta^{\phi}_{i,j} = \frac{{}^{0}b^{\phi}_{i,j:\mathrm{Va}}}{3R} \qquad \text{(Eq 34)}$$

From Eq 33, 34 and considering the values of the coefficients ${}^{k}b^{\phi}_{i,j:\mathrm{Va}}$ reported in Table 6, it follows that $\ln\theta^{\phi}_{E}$ of all solutions varies linearly with composition ($\ln{}^{0}\theta^{\phi}_{i,j} = 0$), except for the HCP and liquid phases of the Hf–Zr system. Specifically, the former shows a positive deviation, whereas the latter exhibits a negative one.

The Hf–Nb diagram (Fig. 5a) is compared with the previous assessment by Fernández Guillermet,[55] while the Hf–Zr diagram (Fig. 5b) is compared with that of

Table 6 Interaction parameters of binary phase solutions modelled in this work

Hf-Nb System	
BCC A2: $(\mathrm{Hf},\mathrm{Nb})_1(\mathrm{Va})_3$	
${}^0\mathrm{L}^{\mathrm{BCC\,A2}}_{\mathrm{Hf,Nb:Va}} = 22713.5$	[55]
${}^0\mathrm{L}^{\mathrm{BCC\,A2}}_{\mathrm{Hf,Nb:Va}} = 22324.1$	This work
${}^1L^{\mathrm{BCC\,A2}}_{\mathrm{Hf,Nb:Va}} = 184.1$	[55]
${}^1L^{\mathrm{BCC\,A2}}_{\mathrm{Hf,Nb:Va}} = 1361.47$	This work
HCP A3: $(\mathrm{Hf},\mathrm{Nb})_1(\mathrm{Va})_{0.5}$	
${}^0L^{\mathrm{HCP\,A3}}_{\mathrm{Hf,Nb:Va}} = 21866.6$	[55]
${}^0L^{\mathrm{HCP\,A3}}_{\mathrm{Hf,Nb:Va}} = 2755.03$	This work
Liquid: $(\mathrm{Hf},\mathrm{Nb})_1$	
${}^0L^{\mathrm{liq}}_{\mathrm{Hf,Nb}} = 11082.8$	[55]
${}^0L^{\mathrm{liq}}_{\mathrm{Hf,Nb}} = 12180$	This work
${}^1L^{\mathrm{liq}}_{\mathrm{Hf,Nb}} = -966.8$	[55]
${}^1L^{\mathrm{liq}}_{\mathrm{Hf,Nb}} = 1413.78$	This work
Hf-Zr System	
BCC A2: $(\mathrm{Hf},\mathrm{Zr})_1(\mathrm{Va})_3$	
${}^0L^{\mathrm{BCC\,A2}}_{\mathrm{Hf,Zr:Va}} = -838.621$	[59]
${}^0L^{\mathrm{BCC\,A2}}_{\mathrm{Hf,Zr:Va}} = -35.3044$	This work
HCP A3:$(\mathrm{Hf},\mathrm{Zr})_1(\mathrm{Va})_{0.5}$	
${}^0L^{\mathrm{HCP\,A3}}_{\mathrm{Hf,Zr:Va}} = 0$	[59]
${}^0L^{\mathrm{HCP\,A3}}_{\mathrm{Hf,Zr:Va}} = -0.0330193 + 0.321454\,T$	This work
$\ln{}^0\theta^{\mathrm{HCP\,A3}}_{\mathrm{Hf,Zr}} = 0.01289$	This work
Liquid: $(\mathrm{Hf},\mathrm{Zr})_1$	
${}^0L^{\mathrm{liq}}_{\mathrm{Hf,Zr}} = 8749.64 - 4.91269\,T$	[59]
${}^0L^{\mathrm{liq}}_{\mathrm{Hf,Zr}} = 5551.68 - 2.83702\,T$	This work
$\ln{}^0\theta^{\mathrm{liq}}_{\mathrm{Hf,Zr}} = -0.11374$	This work

Note that all the values are given as SI unit J/mol formula unit

Bittermann and Rogl.[59] In both cases, an excellent agreement is observed between the present calculations and prior assessments, particularly in reproducing the HCP BCC transformations, the wide solid solubility ranges, and the liquidus/solidus boundaries. The gas phase is included in both diagrams for the sake of completeness. Additionally, the presence of the stoichiometric compound $HfZr_2$, whose thermodynamic description was derived from the third-generation CALPHAD models of Hf and Zr, is shown in Fig. 5b. It is worth mentioning that, due to application of the procedure proposed by He et al.[13], the BCC phase does not re-stabilize at high temperatures even when the gas phase is suspended.

The comparison between the calculated phase diagram and experimental data for the different equilibrium regions are presented in Fig. 6, 7, for the Hf-Nb and Hf-Zr systems, respectively. The black lines correspond to phase equilibria calculated using the third-generation CALPHAD description developed for elemental Hf, Nb, and Zr, prior to any re-adjustment of the binary interaction parameters. Deviations between the black curves and the red dashed lines, which represent previous assessments,[55,59] highlight the influence of the newly adopted third-generation descriptions of the elemental phases.

To improve agreement with the experimental data, binary interaction parameters were subsequently re-optimized. The resulting reassessed phase boundaries are shown as blue curves, demonstrating a satisfactory reproduction of the experimental data across all regions. In the case of the Hf–Nb system, the most significant changes were made to the HCP A3 and liquid phases related parameters, while the interaction parameters for the BCC A2 phase were only slightly modified. For the Hf–Zr system, the liquid and BCC interaction parameters underwent only moderate re-adjustments. However, the most significant change concerns the HCP A3 phase, which now includes a temperature-dependent interaction parameter instead of the temperature-independent and equal to zero value used by Bittermann and Rogl.[59]

This significant change is due to the inclusion of $HfZr_2$ in the phase diagram calculations. To our knowledge, this represents a novel contribution to this study. Indeed, in the previous description of the Hf–Zr system by Bittermann and Rogl,[59] the presence of the intermetallic phase $HfZr_2$ was not considered, as neither theoretical nor experimental indications of its existence were available at that time. Under these conditions (suppressing the intermetallic phase), the interaction parameter ${}^0L^{\mathrm{HCP\,A3}}_{\mathrm{Hf,Zr:Va}}$ of the HCP solid solution could not be negative without violating the third law of thermodynamics.[97–100] In addition, since the experimental data are limited to the high temperature range, a free fitting of ${}^0L^{\mathrm{HCP\,A3}}_{\mathrm{Hf,Zr:Va}}$ based on them would result in a positive value, which, in turn, would imply the presence of a low-temperature miscibility gap in the HCP phase. Such a prediction is inconsistent with the well-established strong chemical affinity and extensive mutual solubility of Hf and Zr. To avoid this contradiction, Bittermann and Rogl fixed ${}^0L^{\mathrm{HCP\,A3}}_{\mathrm{Hf,Zr:Va}}$ equal to zero, even though this choice did not yield the best fit to the experimental data.

In the current assessment, by explicitly considering the presence of $HfZr_2$, the thermodynamic description of the Hf–Zr system is significantly improved. The inclusion of this intermetallic requires a negative of ${}^0L^{\mathrm{HCP\,A3}}_{\mathrm{Hf,Zr:Va}}$ at 0 K to remain consistent with its thermodynamically favored formation and to satisfy the third law of thermodynamics (see also Supplementary material for an extended

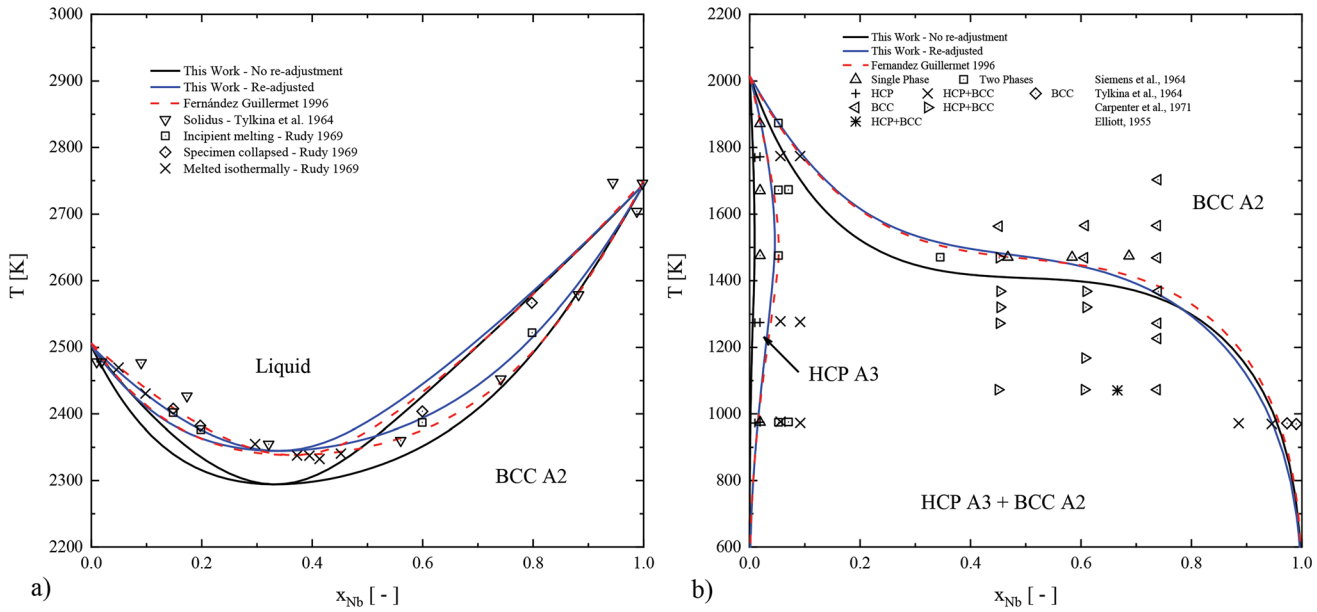

Fig. 6 The equilibrium boundaries of the Hf-Nb phase diagram, calculated using the present thermodynamic description (solid black and blue lines) and the parameters proposed by Fernandez Guillermet[55] (dashed red lines), compared with experimental data: (**a**) BCC A2/Liquid equilibrium boundaries, (**b**) HCP/BCC A2 equilibrium boundaries

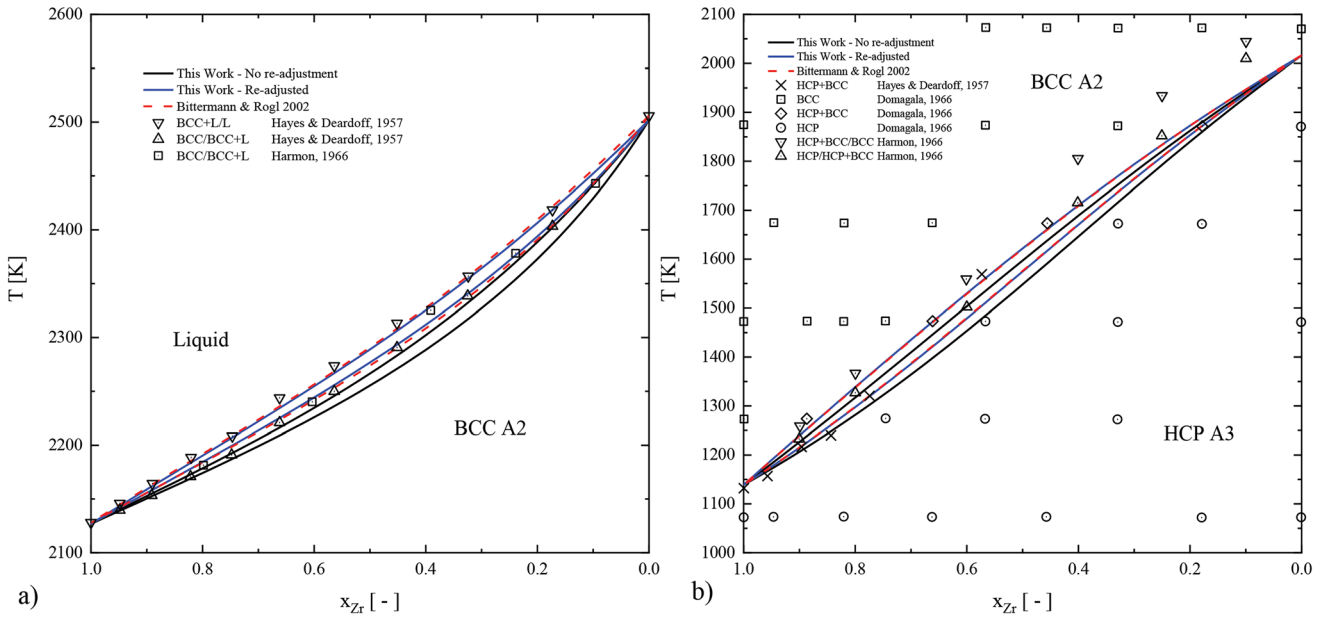

Fig. 7 The equilibrium boundaries of the Hf-Zr phase diagram, calculated using the present thermodynamic description (solid black and blue lines) and the parameters proposed by Bittermann and Rogl[59] (dashed red lines), compared with experimental data: (**a**) BCC A2/Liquid equilibrium boundaries, (**b**) HCP/BCC A2 equilibrium boundaries

discussion of this issue). At the same time, the high-temperature experimental data necessitate a positive ${}^{0}L^{\mathrm{HCP\,A3}}_{\mathrm{Hf,Zr:Va}}$ value to properly reproduce the observed equilibrium with the BCC phase. To reconcile these requirements, ${}^{0}L^{\mathrm{HCP\,A3}}_{\mathrm{Hf,Zr:Va}}$ was expressed as a temperature-dependent linear function, i.e. ${}^{0}L^{\mathrm{HCP\,A3}}_{\mathrm{Hf,Zr:Va}} = a + bT$, where $a < 0$ and $b > 0$. Optimization yielded a negative and small value of a, consistent with the low enthalpy of formation of $HfZr_2$, and a positive value of b, which ensures accurate reproduction of the high-temperature solubility behavior (cf. Table 4 and Fig. 7). This formulation successfully eliminates the occurrence of an artificial miscibility gap in the HCP phase while maintaining consistency with both experimental data and fundamental thermodynamic constraints.

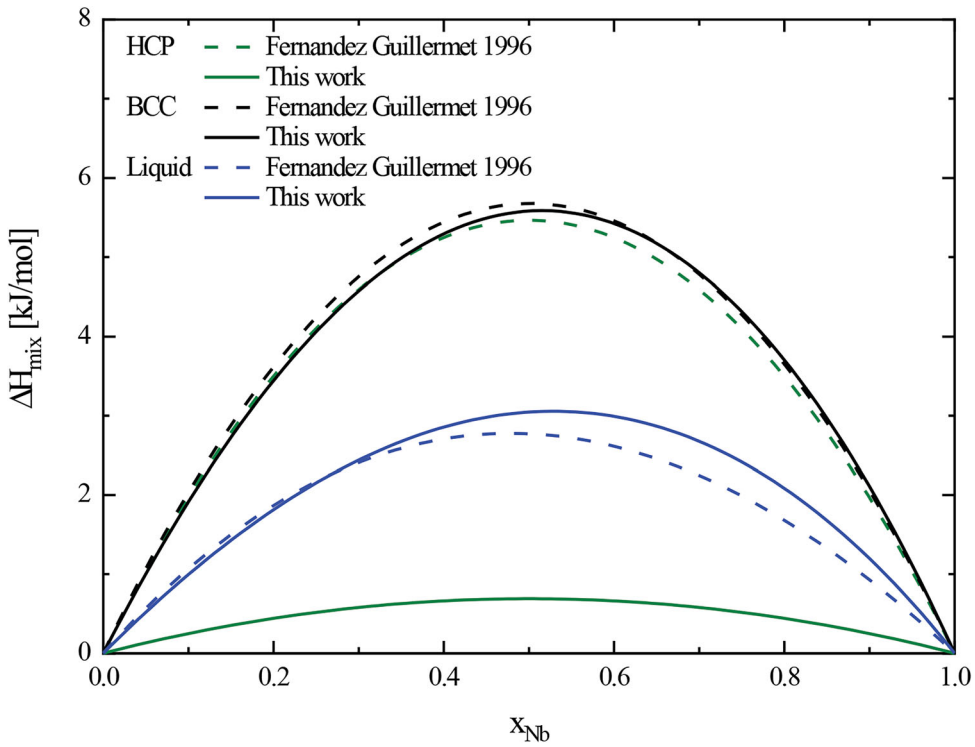

Fig. 8 The enthalpy of mixing (ΔH_{mix}) of Hf-Nb solution phases

Figure 8 illustrates the calculated enthalpy of mixing (ΔH_{mix}) of the HCP, BCC, and liquid phases in the Hf–Nb system, where the results from this work (solid lines) are compared with those of the previous assessment by Fernández Guillermet[55] (dashed lines). It can be clearly seen that the new description significantly reduces, as compared to the previous assessment, the enthalpy of mixing of the HCP across the entire compositional range. As for the BCC phase, only minor differences are observed between the two models, both showing a positive enthalpy of mixing and a maximum near the equiatomic composition. For the liquid phase, the present work predicts slightly lower ΔH_{mix} values than the previous model, especially for Nb-rich solutions.

The calculated Gibbs energy of mixing of Hf–Zr solution phases at 300 K and 1500 K are shown in Fig. 9a and b, respectively. The results are obtained using the updated interaction parameters from this work (solid lines) and compared with those from Bittermann and Rogl[59] (dashed lines). At 300 K (Fig. 9a), the most notable difference is observed for the liquid phase, which is reduced in the updated model across the whole compositional range. It can also be observed that ΔG_{mix}^{EX} of the BCC phase remains low in both descriptions, while the re-optimized model introduces a sign change, causing the transition from slightly negative to slightly positive values. A similar behavior can be seen at 1500 K (Fig. 9b), where the differences become slightly larger.

4.3 Prediction of the Hf–Nb–Zr Ternary Phase Diagram

Based on the reassessed Hf–Nb and Hf–Zr binary systems and their optimized thermodynamic descriptions, the Hf–Nb–Zr ternary phase diagram was predicted still using the third-generation CALPHAD framework. This represents the first thermodynamic assessment of this ternary system, as previous studies were limited to sparse experimental data[33] without any reported CALPHAD modeling. The prediction obtained in the present work offers a detailed view of phase equilibria, including the stability of the BCC A2 and HCP A3 solid solutions, and the behavior of the liquid phase. The selected invariant equilibria for the Hf–Nb–Zr ternary system calculated in this work are summarized in Table 7, while Table 8 reports the critical points of the BCC A2 miscibility gap determined from the predicted ternary diagram.

Figure 10 provides a comprehensive overview of the temperature-dependent stability of the various phases in the Hf–Nb–Zr ternary system. Specifically, Fig. 10a presents an isothermal section at 300 K, at which the stoichiometric intermetallic compound $HfZr_2$ is stable. The two white triangular areas represent three-phase regions composed of BCC A2 (Nb-rich), HCP A3 (Hf- and Zr-rich), and $HfZr_2$. The remaining regions correspond to two-phase equilibria between BCC A2 and HCP A3. Notably, even when the $HfZr_2$ phase is excluded from the model, the calculated 300 K isothermal section does not exhibit extended

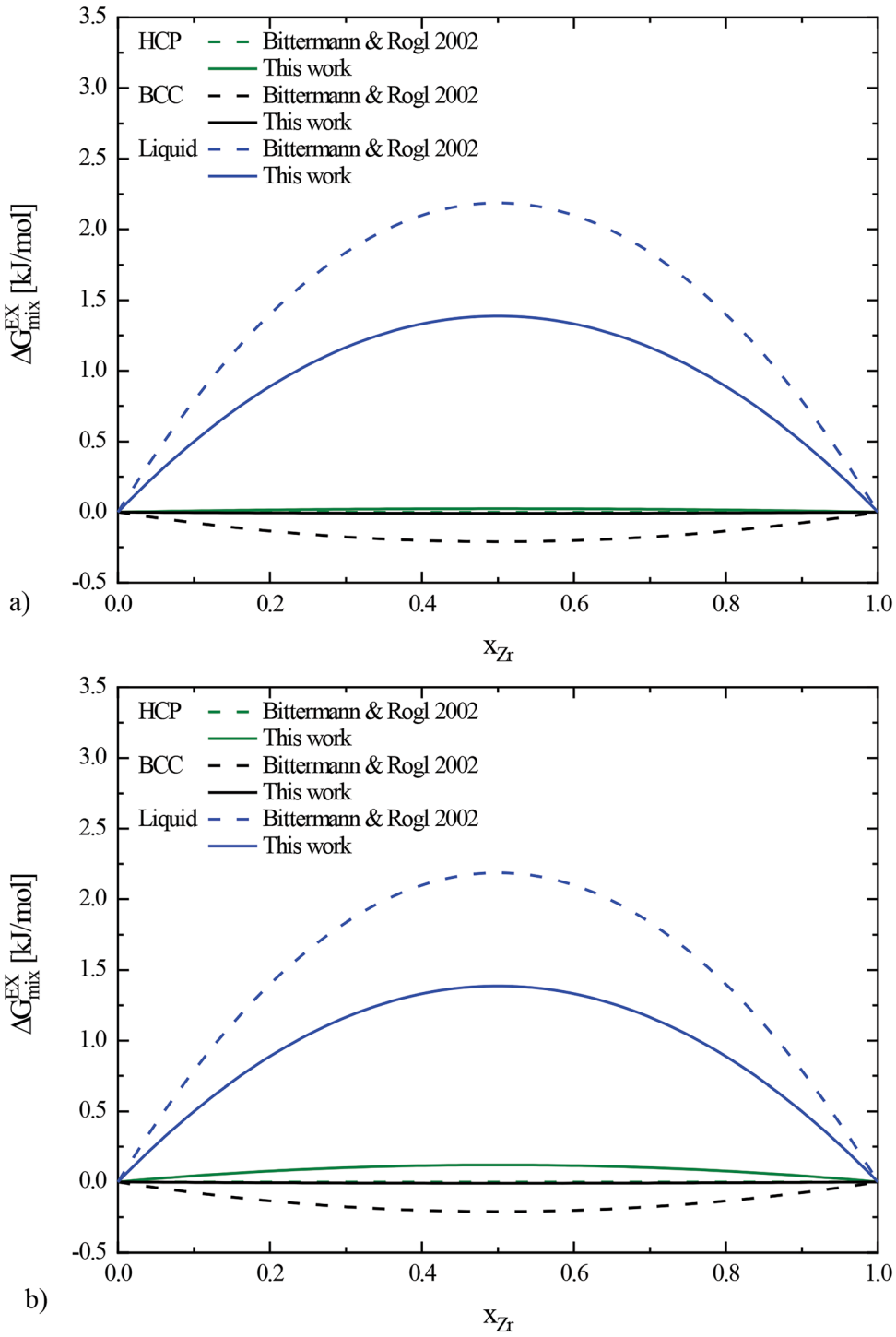

Fig. 9 The Gibbs energy of mixing (ΔG_{mix}^{EX}) of Hf-Zr solution phases: **a**) 300 K and **b**) 1500 K

stable single-phase fields, primarily due to the strong stabilization of the BCC phase of elemental Nb.

The temperature isothermal contours for gas phase formation are shown in Fig. 10b. Zr is the first element to vaporize, with a liquid–gas transition occurring near 4588 K. As temperature increases, the gas-phase field expands toward the Nb-rich side, while pure Nb subsequently ends to vaporize around 5200 K. Figure 10c depicts isothermal contours associated with the formation of the liquid phase. The first appearance of liquid occurs via congruent melting of the BCC A2 solid solution in the Nb–Zr section (at approximately $x_{Nb} \approx 0.2$) around 2014 K,[23] which is notably below the melting point of pure Zr (2127 K). A continuous curve, connecting this point to the lowest melting temperature on the Hf–Nb section ($x_{Nb} \approx 0.37$ at $\approx$ 2338 K), represents the composition-dependent

Table 7 Selected invariant Hf-Nb-Zr equilibria calculated in this work

Reaction (Type)	Phase (i) Composition (1)	(2)	(3)	T [K]
Vap ↔ Liq	Pure Hf	Pure Hf	…	4913.5
	Pure Nb	Pure Nb	…	5199
	Pure Zr	Pure Zr	…	4588
Liq ↔ BCC A2	Pure Hf	Pure Hf	…	2502
	Pure Nb	Pure Nb	…	2745
	Pure Zr	Pure Zr	…	2127
Liq ↔ BCC A2 (Congruent)	$x_{Hf} = 0.660$ $x_{Nb} = 0.340$ $x_{Zr} = 0$	$x_{Hf} = 0.660$ $x_{Nb} = 0.340$ $x_{Zr} = 0$	…	2344.5
	$x_{Hf} = 0$ $x_{Nb} = 0.199$ $x_{Zr} = 0.801$	$x_{Hf} = 0$ $x_{Nb} = 0.199$ $x_{Zr} = 0.801$	…	2014
BCC A2 ↔ HCP A3	Pure Hf	Pure Hf	…	2016
	Pure Zr	Pure Zr	…	1139
HCP A3 ↔ $HfZr_2$ (Congruent)	$x_{Hf} = 1/3$ $x_{Nb} = 0$ $x_{Zr} = 2/3$	$x_{Hf} = 1/3$ $x_{Nb} = 0$ $x_{Zr} = 2/3$	…	461.9
BCC A2 ↔ BCC A2 + HCP A3 (Monotectoid)	$x_{Hf} = 0$ $x_{Nb} = 0.185$ $x_{Zr} = 0.815$	$x_{Hf} = 0$ $x_{Nb} = 0.922$ $x_{Zr} = 0.078$	$x_{Hf} = 0$ $x_{Nb} = 0.000554$ $x_{Zr} = 0.999456$	890

Table 8 Information on the critical points of the BCC A2 phase miscibility gap in the Hf-Nb-Zr ternary phase diagram calculated in this work

T [K]	x_{Hf}	x_{Nb}	x_{Zr}
1249.8	0	0.596	0.404
1309.6	0.342	0.495	0.163

congruent melting line. No BCC A2 phase is stable at temperatures exceeding the melting point of Nb (2745 K).

Finally, the isothermal formation projections of the BCC A2 phase are illustrated in Fig. 10d. The equimolar BCC A2 solid solution becomes stable as a single phase only above 1300 K. On the other hand, at lower temperatures and intermediate compositions, particularly in the Hf-rich portion, the BCC A2 phase is destabilized by the emergence of a miscibility gap. This results in a two-phase region (BCC_1+ BCC_2), bounded by the blue curve tracing the binodal line. As summarized in Tables 7 and 8, this miscibility gap exists between approximately 900 K and 1351.5 K, depending on composition.

Figure 11a and b present the predicted isothermal sections of the Hf–Nb–Zr ternary phase diagram at 1273 K and 1973 K, compared with the experimental data from Fedorov et al.,[33] which are, at the best of authors' knowledge, the only ones reported in the literature for this system. The theoretical predictions are first illustrated and a discussion about their comparison with the experimental data will then follow. At 1000 °C (Fig. 11a), the model predicts a narrow HCP A3 single-phase field along the Hf–Zr side, a BCC A2 single-phase region that covers the Hf-poor composition domain, a dominant HCP + BCC two-phase region in the Hf-rich part, a BCC miscibility gap (BCC_1+BCC_2) extending into intermediate compositions, and a small, albeit distinct, three-phase field (HCP + BCC_1+ BCC_2). In contrast, a broad single-phase BCC A2 field across nearly the entire diagram, with HCP stability limited to the Hf-rich corner, is predicted by the model at 1700 °C (Fig. 11b).

The experimental data reported by Fedorov et al.[33] which are shown in Fig. 11 were obtained by annealing of different samples at 1000 °C and 1700 °C, followed by metallographic examinations of the quenched alloys. The data points are classified based on the phases identified post-quenching. Specifically, black points correspond to compositions where a single-phase BCC structure was observed, primarily located toward the Nb-rich side of the diagram. Green data, which indicate regions of single-phase HCP structure concentrated near the Hf–Zr-rich edge, reflect the low-temperature stability of HCP for pure Hf and Zr. Finally, red dots denote alloys whose phase transformations during quenching resulted in mixed BCC and HCP microstructures.

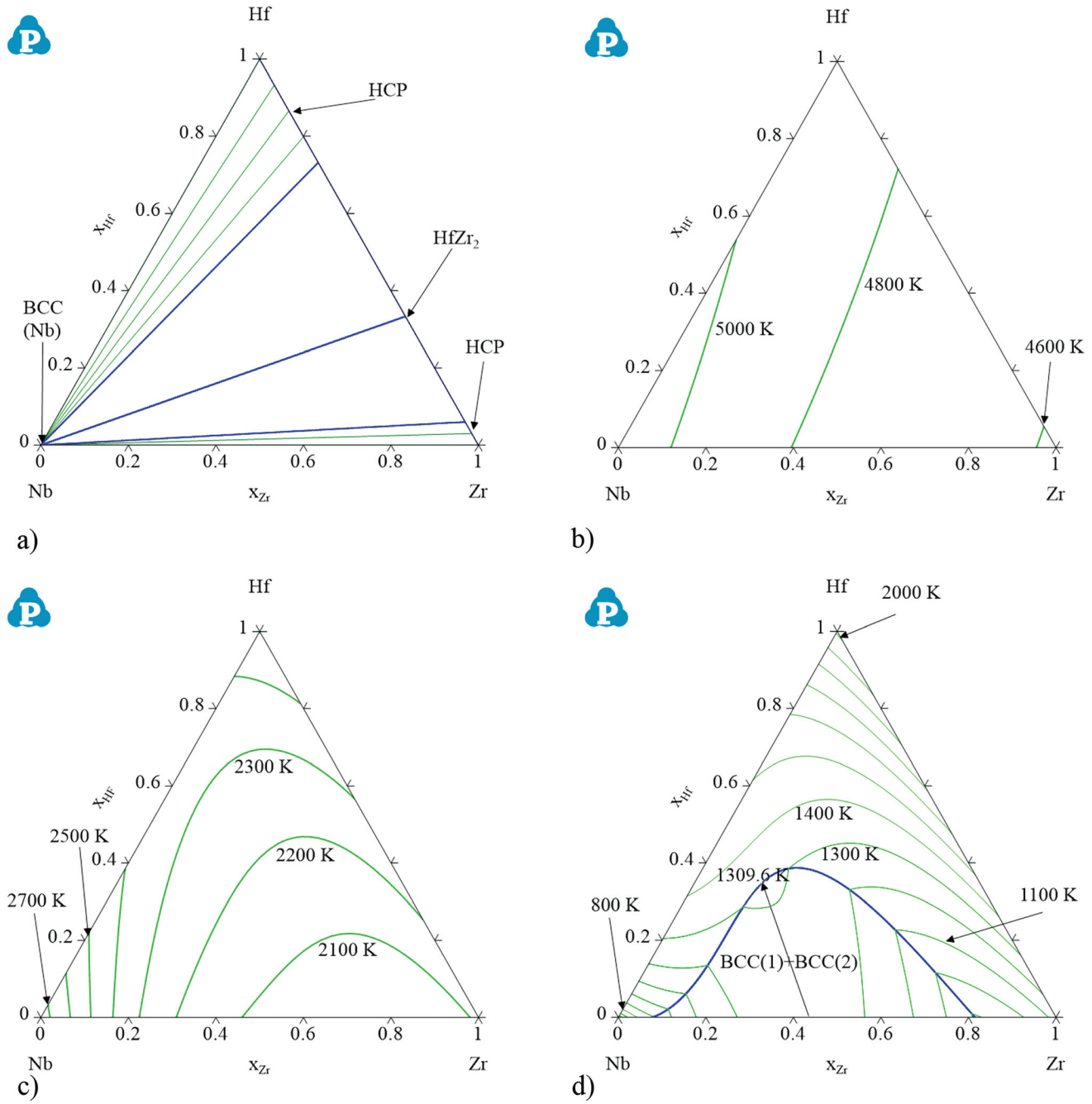

Fig. 10 Hf-Nb-Zr ternary phase diagram: (**a**) isothermal section at 300 K; (**b**) isothermal gas phase formation projections (stable liquid phase on the left); (**c**) isothermal liquid phase formation projections (from the right bottom liquid phase forms as the temperature increases); (**d**) isothermal BCC phase formation projections (blue curve indicates the invariant equilibria depending on temperature due to the presence of the miscibility gap)

By comparing the thermodynamic description results and the experimental data just discussed, it can be clearly seen that, while some experimental points support the theoretical results (black points in both Figures and some red data in Fig. 11a), several other biphasic (red) points and the single HCP phase (green) data fall within regions where the model predicts the presence of the BCC single-phase. On the one hand, this could imply that the proposed thermodynamic assessment overestimates the high-temperature stability range of the BCC phase. On the other hand, the experimentally inferred persistence of the HCP phase at these high temperatures appears inconsistent, as none of the constituent elements exhibits HCP stability under such conditions.

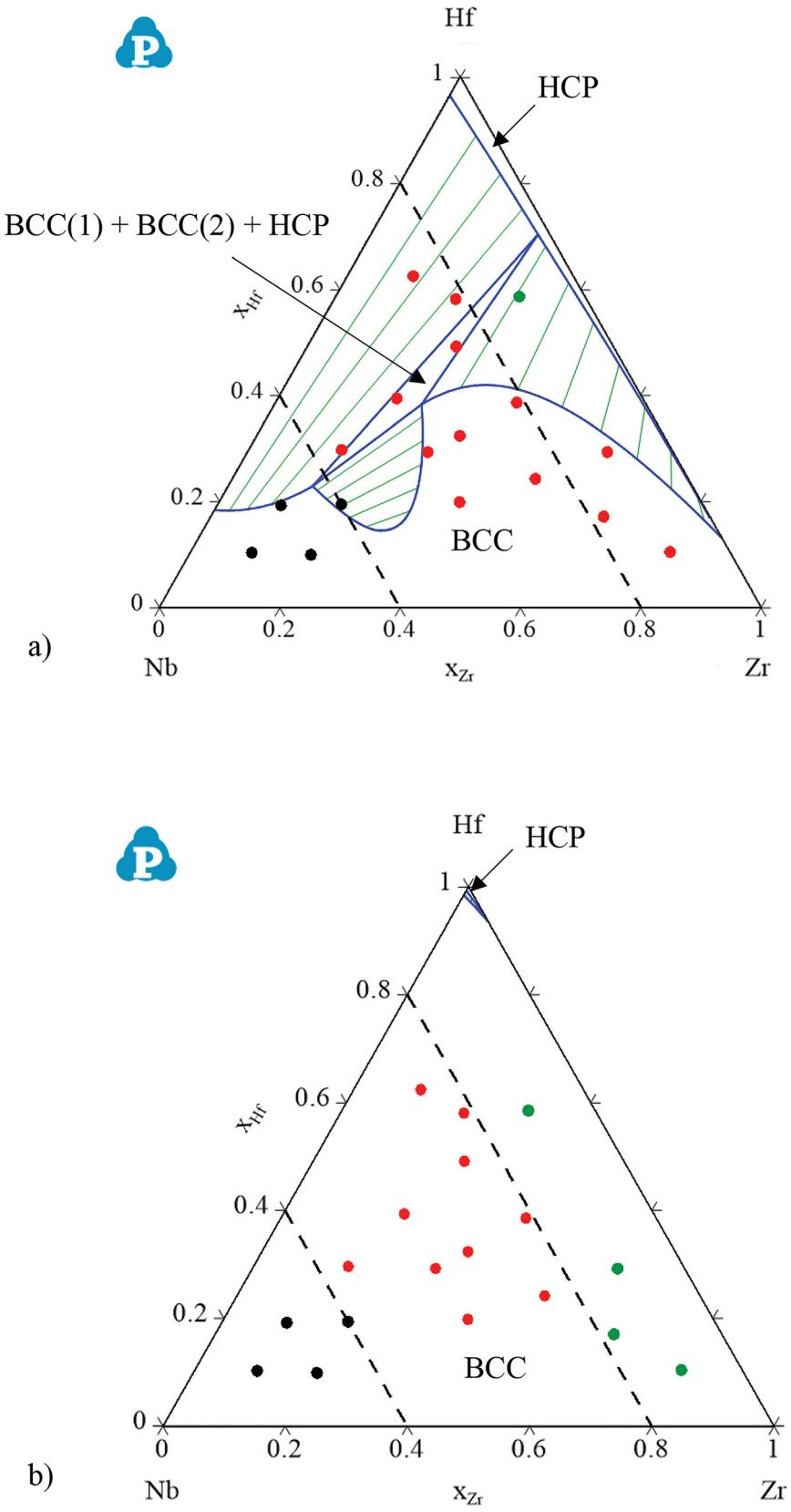

Fig. 11 Hf-Nb-Zr Ternary phase diagram: isothermal section at **a**) 1273 K; **b**) 1973 K. Data from Fedorov et al.[33] : BCC (black dots), BCC + HCP (red dots) and HCP (green dots)

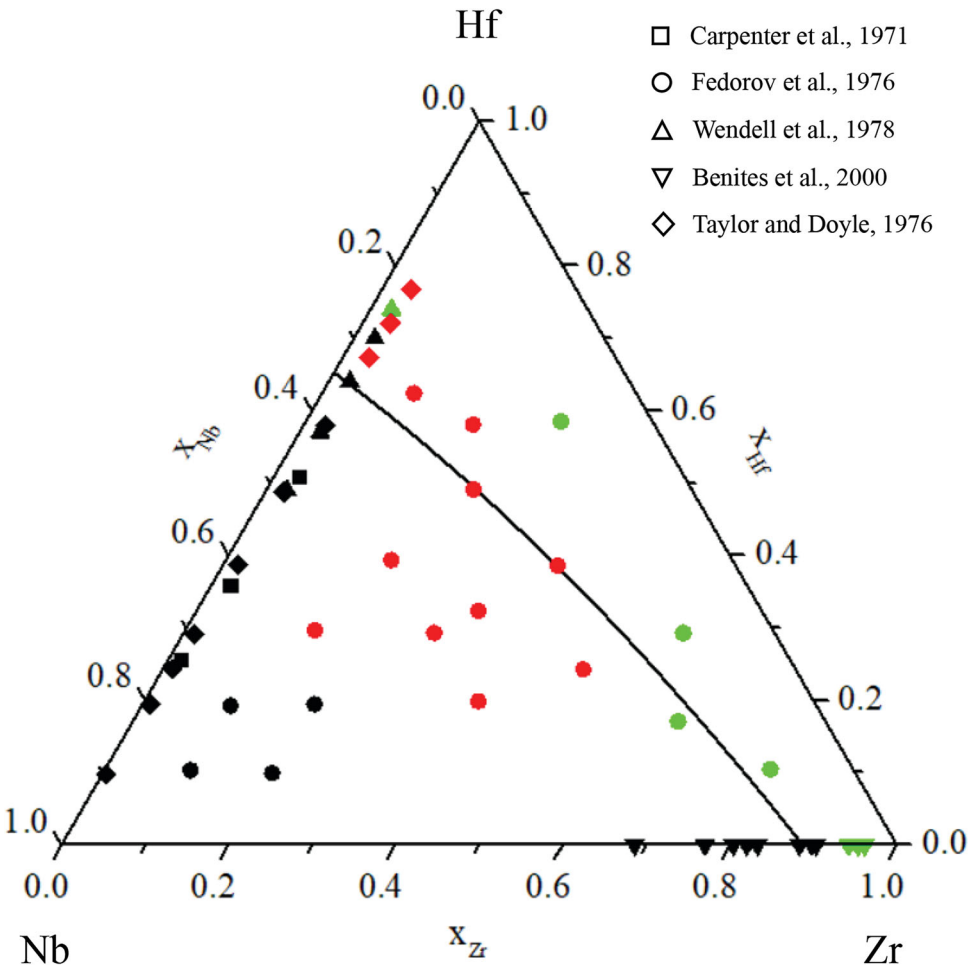

Fig. 12 Ternary Hf–Nb–Zr phase diagram showing the loci of compositions for which the equilibrium temperature T_0 equals room temperature (black curve). The curve separates the Nb-rich region, where T_0 is below room temperature and the Hf- and Zr-rich region, where the BCC → HCP martensitic transformation is expected to occur. Experimental data from literature are also reported for validation. Black symbols denote compositions retaining the BCC phase after quenching, red symbols indicate dual-phase (BCC + HCP) products, and green symbols correspond to complete transformation to the HCP structure

It is worth pointing out that, as far as the experimental data are concerned, their reliability is uncertain. Importantly, Fedorov et al.'s own interpretation supports the extensive high-temperature stability of BCC,[33] emphasizing that the discrepancies with the quenched structures primarily reflect kinetic limitations associated with transformations taking place during cooling rather than a fundamental thermodynamic disagreement. Specifically, it was reported that the high-temperature BCC single-phase could not be retained upon quenching in alloys containing less than 60 at.% niobium, while this phase was not observed at all at 1700 °C in alloys with less than 20 at.% Nb (see dashed lines in Fig. 11).

This finding may be ascribed to the peculiar BCC-to-HCP martensitic transformations taking place in β-Zr-based alloys and, likely, in β-Hf-based ones.[101,102] To perform a comprehensive analysis, the T_0 value as a function of composition was calculated based on the revised thermodynamic description of this system. The temperature T_0 is defined as the temperature at which the Gibbs energies of the parent (BCC) and product (HCP) phases are equal, i.e., $G^{\mathrm{BCC}}(T) = G^{\mathrm{HCP}}(T)$. It therefore represents the limiting temperature below which the diffusionless martensitic transformation becomes thermodynamically favorable. The locus of compositions for which T_0 equals room temperature was then determined.

The results of these calculations are represented by the black curve shown in Fig. 12. This curve divides the diagram into two regions. On its left side (the Nb-rich part of the diagram) lie the compositions whose T_0 values are lower than room temperature. Therefore, the corresponding high-temperature BCC (β) phase can, at least in principle, be preserved if sufficiently fast quenching is applied. This occurs because the diffusion-less martensitic transformation to the low-temperature HCP (α') phase cannot take place. In contrast, this transformation is theoretically expected to occur for all compositions located on the right side of the black curve (the Hf- and Zr-rich region).

To verify the consistency of the derived thermodynamic description, a comparison with experimental data is also provided in Fig. 12. Specifically, available data related to the high-temperature β phase obtained after annealing and the corresponding phase observed after quenching or rapid cooling are collected. In this analysis, the data reported by

Fedorov et al.[33] as well as experimental information concerning the binary systems Hf–Nb[84,103,104] and Nb–Zr[105] are included. It should be noted that, in the case of the Hf–Nb system, a significant amount of Zr was also present. The interpretation of the symbol colors is the same as described for Fig. 11. Experimental black points (retained β) cluster in the Nb-rich region while green points (fully α') lie predominantly in the Hf/Zr-rich region. On the binary sides, datasets align closely with the calculated partition: Nb-rich alloys predominantly retain β, Hf/Zr-rich alloys transform to α'.

As a general conclusion for the Hf-Nb system, already given by Taylor and Doyle,[103] it appears that the transformation of the diffusion-less martensitic type induced by quenching cannot be avoided in Nb-poor alloys. However, the progressive addition of Nb lowers the transformation temperatures and slows down the reaction rate, such that when $x_{Nb} \gtrsim 0.75$ it becomes possible to retain the β phase.[103] In the case of the binary Nb-Zr, the required amount of Nb to suppress the martensitic transformation appears to be smaller.

Nevertheless, two groups of inconsistencies with the calculated T_0 can be identified. Specifically, minor deviations appear close to the calculated boundary. These include isolated red points where a single phase would be expected, and some black or green points misplaced with respect to the dividing line. Such discrepancies might be readily explained by experimental uncertainties and kinetic effects. Small differences in actual composition, grain size, or cooling rate can easily shift the martensite start temperature, M_s, by a few tens of kelvin, leading to either incomplete or premature transformation. Furthermore, by considering the not so recent literature sources, classifying a microstructure as "dual" or "single" phase could have been affected by the detection threshold used in each experimental study.

The major inconsistencies regarding the Fedorov et al. data correspond to intermediate Nb contents,[33] where several red points lie far inside the predicted β-metastability domain. According to the present thermodynamic model, these alloys should exhibit T_0 lower than room temperature and thus retain the β structure after quenching. Their partial transformation is therefore unexpected and likely reflects extrinsic factors, most probably insufficient quenching rates, local segregation, or uncertainties in reported compositions, that reduced the effective metastability of the β phase.

Despite the generally good agreement between the calculated T_0 partition and most literature data, the inconsistencies observed in the intermediate Nb-rich composition range, especially those reported by Fedorov et al.[33], highlight the limited and somewhat heterogeneous nature of the available experimental information. The scarcity of more recent systematic quenching studies for the ternary system Hf-Nb-Zr and performed under well-controlled thermal conditions makes it difficult to unambiguously determine whether these deviations arise from kinetic effects, compositional inaccuracies, or intrinsic limitations of the proposed thermodynamic description.

Therefore, new experimental investigations are strongly needed to clarify the stability of the β phase in the intermediate Nb-rich domain. Controlled annealing and rapid-quenching experiments, possibly combined with in situ high-temperature diffraction or microstructural characterization, would be particularly valuable to confirm whether the β phase can indeed be retained metastably or if partial martensitic transformation occurs under realistic cooling rates. Such data would provide a critical benchmark for validating and refining the present thermodynamic description of the Hf–Nb–Zr system and for improving the predictive accuracy of future CALPHAD assessments in related refractory alloy systems.

5 Conclusions

In this work, the third-generation CALPHAD approach has been first extended to provide a refined thermodynamic description of elemental hafnium. This includes not only the stable HCP and BCC phases, but also a complete modeling of the metastable FCC and liquid phases. The advanced treatment of the liquid phase allows for a better representation of its temperature-dependent heat capacity, including the non-linear behavior near and above the melting point, which deviates from the constant heat capacity assumption traditionally used in second-generation models.

The newly developed third-generation descriptions for Hf, Nb, and Zr have been then used to reassess the binary Hf–Nb and Hf–Zr systems. Notably, the modeling of the Hf–Zr system also comprises the intermetallic $HfZr_2$ compound, which had not been accounted for in earlier assessments. This inclusion allowed for the reassessment of interaction parameters, particularly for the HCP solid solution, in a way that satisfies the third law of thermodynamics and reflects both low-temperature phase formation and the high-temperature equilibria of the HCP one.

Based on these binary descriptions, the Hf–Nb–Zr ternary phase diagram has been finally predicted using third-generation models. The obtained outcomes successfully capture key topological features such as the BCC miscibility gap and three-phase regions involving BCC_1, BCC_2, and HCP phases. Comparisons with the only available experimental isothermal sections from Fedorov et al. reveal reasonable agreement particularly for Nb-rich compositions, while larger discrepancies are evident in the

case of alloy with less than 60 at.% of niobium.[33] These differences can be largely attributed to some experimental limitations associated with the quenching procedure used in that study, which was apparently unable to retain the high-temperature structures. High-quality ternary data with improved kinetic control in experimental studies are then urgently needed to further validate the thermodynamics of this refractory system.

Supplementary Information The online version contains supplementary material available at https://doi.org/10.1007/s11669-026-01230-w.

Acknowledgments One of the authors (Mariano Casu) performed his activity in the framework of the Ph.D. in Innovation Sciences and Technologies at the University of Cagliari, Italy.

Funding Open access funding provided by Università degli Studi di Cagliari within the CRUI-CARE Agreement. This work has been developed within the framework of the project eINS-Ecosystem of Innovation for Next Generation Sardinia (cod. ECS 00000038), funded by the Italian Ministry for Research and Education (MUR) under the National Recovery and Resilience Plan (PNRR)—MISSION 4 COMPONENT 2, "From research to business" INVESTMENT 1.5, "Creation and strengthening of Ecosystems of innovation" and construction of "Territorial R&D Leaders". Italian Ministry also funded this research for Research and Education (MUR) under the National Recovery and Resilience Plan (NRRP), Mission 4, Component 2, Investment 1.1, Call for tender No. 104 published on 2.2.2022 by the Italian Ministry of University and Research (MUR), funded by the European Un-ion—NextGenerationEU—Project Title I-CREATE—Innovative Class of REfrAcTory ceramics for extreme Environments—CUP F53D23002020006—Grant Assignment Decree No. 104 adopted on 2 February 2022 by the Italian Ministry of Ministry of University and Research (MUR).

References

1. T.C. Dube and J. Zhang, Underpinning the Relationship Between Synthesis and Properties of High Entropy Ceramics: A Comprehensive Review on Borides, Carbides and Oxides, *J. Eur. Ceram. Soc.*, 2024, **44**(3), p 1335–1350.
2. T. Qureshi, M.M. Khan, and H.S. Pali, Review: High-Entropy Borides—Challenges and Opportunities, *J. Mater. Sci.*, 2024, **59**(34), p 15921–15991.
3. P.C. Verma, S.K. Tiwari, A. Saurabh, and A. Manoj, Recent Advances in High-Entropy Ceramics: Synthesis Methods, Properties, and Emerging Applications, *Ceramics*, 2024, **7**(4), p 1365–1389.
4. M. Shojaie-bahaabad, M. Bozorg, M. Najafizadeh, and P. Cavaliere, Ultra High Temperature Ceramic Coatings in Thermal Protection Systems (TPS), *Ceram. Int.*, 2024, **50**(7), p 9937–9951.
5. K.A. Kane, B.A. Pint, D. Mitchell, and J.A. Haynes, Oxidation of Ultrahigh Temperature Ceramics: Kinetics, Mechanisms, and Applications, *J. Eur. Ceram. Soc.*, 2021, **41**(13), p 6130–6150.
6. A. Nisar, R. Hassan, A. Agarwal, and K. Balani, Ultra-High Temperature Ceramics: Aspiration to Overcome Challenges in Thermal Protection Systems, *Ceram. Int.*, 2022, **48**(7), p 8852–8881.
7. L. Backman, J. Gild, M. Qin, J. Luo, and E.J. Opila, Composition Dependence of Oxidation Resistance In High Entropy Ultra-High Temperature Ceramics, *Open Ceram.*, 2024, **18**, p 100563.
8. L. Backman, B.M. Hunter, M.L. Weaver, and E.J. Opila, The Oxidation Kinetics and Mechanisms Observed during Ultra-High Temperature Oxidation of (HfZrTiTaNb)C and (HfZrTiTaNb)B_2, *J. Appl. Phys.*, 2024, **136**(5), p 055106.
9. Y. Xu, L. Yu, T. Zhao, X. Zhong, J.-X. Liu, G.-J. Zhang, Y. Niu, and X. Zheng, Composition Design of Oxidation Resistant Non-Equimolar High-Entropy Ceramic Materials: An Example of (Zr–Hf–Ta–Ti)B_2 Ultra-High Temperature Ceramics, *J. Adv. Ceram.*, 2024, **13**(12), p 2087–2100.
10. Q. Guo, H. Ying, B. Yuan, H. Fan, L. Hua, R. Liu, and J. Wang, Preparation and Properties of Ta Fiber Reinforced High-Entropy ($Ti_{0.2}Zr_{0.2}Hf_{0.2}Nb_{0.2}Ta_{0.2}$)$B_2$-SiC Composite Ceramics, *Ceram. Int.*, 2024, **50**(24), p 56070–56085.
11. Z. Tang, Z. Wen, Y. Liu, L. Zhuang, H. Yu, and Y. Chu, Rapid Experimental Screening of High-Entropy Diborides for Superior Oxidation Resistance, *Adv. Func. Mater.*, 2024, **34**(12), p 2312239.
12. N. Saunders, and A.P. Miodownik, *CALPHAD calculation of phase diagrams: a comprehensive guide*. Elsevier, Pergamon, 1998.
13. Z. He, Q. Chen, and M. Selleby, Third Generation Calphad for Key Elements, *J. Phase Equil. Diffus.*, 2024, **45**(6), p 1163–1181.
14. J. Vřešťál, J. Pavlů, U.D. Wdowik, and M. Šob, Modelling of Phase Equilibria in the Hf-V System Below Room Temperature, *J. Min. Metall., Sect. B: Metall.*, 2017, **53**(3), p 239–247.
15. S. Bigdeli and M. Selleby, A Thermodynamic Assessment of the Binary Fe-Mn System for the Third Generation of Calphad Databases, *Calphad*, 2019, **64**, p 185–195.
16. A. Dinsdale, O. Zobac, A. Kroupa, and A. Khvan, Use of Third Generation Data for the Elements to Model the Thermodynamics of Binary Alloy Systems: Part 1–The Critical Assessment of Data for the Al-Zn System, *Calphad*, 2020, **68**, p 101723.
17. B. Hu, S. Sridar, L. Hao, and W. Xiong, A New Thermodynamic Modeling of the Ti–V System Including the Metastable ω Phase, *Intermetallics*, 2020, **122**, p 106791.
18. L. Hao, A. Ruban, and W. Xiong, CALPHAD Modeling based on Gibbs Energy Functions from Zero Kevin and Improved Magnetic Model: A Case Study on the Cr–Ni System, *Calphad*, 2021, **73**, p 102268.
19. Z. He, B. Kaplan, H. Mao, and M. Selleby, The Third Generation Calphad Description of Al–C Including Revisions of Pure Al and C, *Calphad*, 2021, **72**, p 102250.
20. Z. He and M. Selleby, A Third Generation Calphad Description of W-C Including a Revision of Liquid C, *Calphad Comput. Coupl. Phase Diag. Thermochem.*, 2022, **78**, p 102449.

21. E. Zhang, X. Xu, Y. Chen, and Y. Tang, Third-Generation Thermodynamic Descriptions for Ta-Cr and Ta-V Binary Systems, *Materials*, 2022, **15**(6), p 2074.
22. L. Hao, S. Bigdeli, and W. Xiong, From Zero Kelvin Upwards: Thermodynamic Modeling of the Mn-Ni System with Third Generation Calphad Models, *J. Phase Equilib. Diffus.*, 2024, **45**(6), p 1182–1193.
23. G. Traversari, M. Casu, R. Orrù, A. Cincotti, A. Concas, G. Cao, and A.M. Locci, Third-Generation CALPHAD Modeling of Elemental Nb and Zr and Partial Re-Assessment of Their Binary Phase Diagram, *Materials*, 2024, **17**(23), p 5978.
24. O. Zobac, A. Kroupa, and A. Dinsdale, Use of Third Generation Data for the Pure Elements to Model the Thermodynamics of Binary Alloy Systems: Part 3–The Theoretical Prediction of the Al–Si–Zn System, *Calphad*, 2024, **87**, p 102742.
25. L. Hao, C. Shen, N.M. Fortunato, H. Zhang, and W. Xiong, Third Generation Calphad: Thermodynamic Assessment of the Ni-Ga System with Physics-Based Models, *Calphad*, 2025, **88**, p 102797.
26. K. Kaboli and S. Bigdeli, SFE Assessment of Fe–Mn Binary System Using the 3rd Generation Calphad Database: Phase Diagram Re-assessment and Physical Insights, *J. Phase Equil. Diffus.*, 2025, **46**(2), p 134182.
27. W. Ma, J. Gebauer, A.K. Czerny, M.R. Chegeni, I. Gallino, R. Busch, and H.J. Seifert, Thermodynamic Assessment of the Sulfur and the Nickel-Sulfur Systems, *Calphad Comput. Coupl. Phase Diag. Thermochem.*, 2025, **89**, p 102821.
28. E. Zhang, Y. Tang, M. Wen, A. Obaied, I. Roslyakova, and L. Zhang, On Phase Stability of Mo-Nb-Ta-W Refractory High Entropy Alloys, *Int. J. Refract Metal Hard Mater.*, 2022, **103**, p 105780.
29. A. Walnsch, A. Leineweber, and M.J. Kriegel, A Third Generation CalPhaD Assessment of the Fe–Mn–Ti System Part I: The Binary Subsystems Fe–Mn, Fe–Ti and Mn–Ti, *Calphad Comput. Coupl. Phase Diag. Thermochem.*, 2023, **81**, p 102555.
30. A. Walnsch, A. Leineweber, and M.J. Kriegel, A Third Generation CalPhaD Assessment of the Fe–Mn–Ti System Part II: The Ternary System Fe–Mn–Ti, *Calphad*, 2023, **81**, p 102553.
31. J. Vřešťál, J. Štrof, and J. Pavlů, Extension of SGTE Data for Pure Elements to Zero Kelvin Temperature—A Case Study, *Calphad*, 2012, **37**, p 37–48.
32. J. Pavlů, P. Řehák, J. Vřešťál, and M. Šob, Combined Quantum-Mechanical and Calphad Approach to Description of Heat Capacity of Pure Elements Below Room Temperature, *Calphad*, 2015, **51**, p 161–171.
33. T.F. Fedorov, R.V. Popova, R.V. Skolozdra, Solid Solutions in the Zr-Nb-Hf System, *Russian metallurgy*, 1967, 109-111.
34. J.W. Arblaster, Thermodynamic Properties of Hafnium, *J. Phase Equil. and Diffus.*, 2014, **35**(4), p 490–501.
35. N.H. Paulson, E. Jennings, and M. Stan, Bayesian Strategies for Uncertainty Quantification of the Thermodynamic Properties of Materials, *Int. J. Eng. Sci.*, 2019, **142**, p 74–93.
36. H.K. Adenstedt, Physical, Thermal and Electrical Properties of Hafnium and High Purity Zirconium, *Trans. Am. Soc. Met.*, 1952, **44**, p 949–973.
37. N.M. Wolcott, The Atomic Heats of Titanium, Zirconium and Hafnium, *Philos. Mag.*, 1957, **2**(22), p 1246–1254.
38. D.L. Burk, I. Estermann, and S.A. Friedberg, The Low Temperature Specific Heats of Titanium, Zirconium and Hafnium, *Zhurnal Phys. Chem.*, 1958, **16**, p 183–193.
39. G.D. Kneip Jr., J.O. Betterton Jr., and J.O. Scarbrough, Low-Temperature Specific Heats of Titanium, Zirconium, and Hafnium, *Phys. Rev.*, 1963, **130**(5), p 1687.
40. T. A. McClaine, Thermodynamic and Kinetic Studies for a Refractory Materials Program, Technical Report No. ASD-TDR-62-204 (Pt. II). LITTLE (ARTHUR D) INC CAMBRIDGE MA, 1964.
41. E.W. Collings and J.C. Ho, Magnetic-Susceptibility and Low-Temperature Specific-Heat Studies of Ti, Zr, and Hf, *Phys. Rev. B*, 1971, **4**(2), p 349–356.
42. L.P. Filippov and R.P. Yurchak, High-Temperature Investigations of the Thermal Properties of Solids, *J. Eng. Phys.*, 1971, **21**, p 1209–1220.
43. V.E. Peletskii and V.P. Druzhinin, Experimental Study of Some Physical Properties of Hafnium at High Temperatures, *Teplofiz. Vys. Temp.*, 1971, **9**(3), p 539–545.
44. A.V. Arutyunov, S.N. Banchila, and L.P. Filippov, Thermal, Electrical and Emissive Properties of Hf in the High-Temperature Region, *High Temp.*, 1972, **10**(2), p 375–377.
45. A. Cezairliyan and J.L. McClure, Simultaneous Measurements of Specific Heat, Electrical Resistivity, and Hemispherical Total Emittance by a Pulse Heating Technique: Hafnium–3 (wt.%) Zirconium, 1500 to 2400 K, *J. Res. National Bureau Stand A*, 1975, **79**(2), p 431–436.
46. N.D. Milošević and K.D. Maglić, Thermophysical properties of solid phase hafnium at high temperatures, *Int. J. Thermophys.*, 2006, **27**, p 530–553.
47. I. B. Fieldhouse and J. I. Lang, Measurement of Thermal Properties, Technical Report, Armour Research Foundation Chicago IL, 1961
48. D.T. Hawkins, M. Onillon, and R.L. Orr, High-Temperature Heat Content of Hafnium, *J. Chem. Eng. Data*, 1963, **8**(4), p 628–629.
49. Y.A. Golutvin and E.G. Maslennikova, The Heat Capacity of Metallic Hafnium, *Russ. Metall. Met.*, 1970, **5**, p 129–135.
50. S. Kats, Thermophysical Properties of Zirconium and Hafnium at High Temperatures, *Teplofiz. Vys. Temp.*, 1985, **23**(2), p 395–397.
51. C. Cagran, T. Hüpf, B. Wilthan, and G. Pottlacher, Selected Thermophysical Properties of Hf-3% Zr from 2200 K to 3500 K Obtained by a Fast Pulse-Heating Technique, *High Temp. High Press.*, 2008, **37**(3), p 1.
52. P.F. Paradis, T. Ishikawa, and S. Yoda, Non-Contact Measurements of the Thermophysical Properties of Hafnium-3 mass% Zirconium at High Temperature, *Int. J. Thermophys.*, 2003, **24**(1), p 239–258.
53. M. Rösner-Kuhn, K. Drewes, H. Franz, and M.G. Frohberg, Enthalpy Measurements of the Solid High-Temperature β-Phase of Titanium and Zirconium by Levitation Drop Calorimetry, *J. Alloys Compd.*, 2001, **316**(1–2), p 175–178.
54. V.N. Korobenko, O.A. Polyakova, and A.I. Savvatimskii, Heat Capacity of Liquid Hafnium from the Melting Point to the Boiling Point at Atmospheric Pressure, *High Temp.*, 2005, **43**(1), p 38–44.
55. A. Fernández-Guillermet, Gibbs Energy Coupling of Phase Stability and Thermochemistry in the Hf-Nb System, *J. Alloys Compd.*, 1996, **234**(1), p 111–118.
56. G. Ghosh, A. Van de Walle, M. Asta, and G.B. Olson, Phase Stability of the Hf-Nb System: From First-Principles to CALPHAD, *Calphad Comput. Coupl. Phase Diag. Thermochem.*, 2002, **26**(4), p 491–511.
57. A.T. Dinsdale, SGTE Data for Pure Elements, *Calphad*, 1991, **15**(4), p 317–425.
58. J.P. Abriata, J.C. Bolcich, and H.A. Peretti, The Hf−Zr (Hafnium−Zirconium) System, *Bulletin Alloy Phase Diag.*, 1982, **3**, p 29–34.
59. H. Bittermann and P. Rogl, Critical Assessment and Thermodynamic Calculation of the Ternary System C-Hf-Zr (Carbon-Zirconium-Hafnium), *J. Phase Equil.*, 2002, **23**(3), p 218.
60. H. Hosono, K. Tanabe, E. Takayama-Muromachi, H. Kageyama, S. Yamanaka, H. Kumakura, and S. Fujitsu,

Exploration of New Superconductors and Functional Materials, and Fabrication of Superconducting Tapes and Wires of Iron Pnictides, *Sci. Technol. Adv. Mater.*, 2015, **16**(3), p 033503.
61. A. Kumar, R. Sharma, and N. Singh, Quantum Oscillations in Stoner Susceptibility: A Theory, *J. Magn. Magn. Mater.*, 2019, **487**, p 165302.
62. O. Levy, G.L.W. Hart, and S. Curtarolo, Hafnium Binary Alloys from Experiments and First Principles, *Acta Mater.*, 2010, **58**(8), p 2887–2897.
63. J.E. Saal, S. Kirklin, M. Aykol, B. Meredig, and C. Wolverton, Materials Design and Discovery with High-Throughput Density Functional Theory: The Open Quantum Materials Database (OQMD), *JOM*, 2013, **65**, p 1501–1509.
64. S. Kirklin, J.E. Saal, B. Meredig, A. Thompson, J.W. Doak, M. Aykol, S. Rühl, and C. Wolverton, The Open Quantum Materials Database (OQMD): Assessing the Accuracy of DFT Formation Energies, *npj Comput. Mater.*, 2015, **1**, p 15010.
65. H.C. Wang, S. Botti, and M.A.L. Marques, Predicting Stable Crystalline Compounds using Chemical Similarity, *NPJ Comput. Mater.*, 2021, **7**, p 12.
66. T. Nagase, S. Anada, P.D. Rack, J.H. Noh, H. Yasuda, H. Mori, and T. Egami, Electron-Irradiation-Induced Structural Change in Zr-Hf-Nb Alloy, *Intermetallics*, 2012, **26**, p 122–130.
67. T. Nagase, S. Anada, P.D. Rack, J.H. Noh, H. Yasuda, H. Mori, and T. Egami, MeV Electron-Irradiation-Induced Structural Change in the bcc Phase of Zr-Hf-Nb Alloy with an Approximately Equiatomic Ratio, *Intermetallics*, 2013, **38**, p 70–79.
68. M. Schick, A. Watson, M. to Baben, and K. Hack, A Modified Neumann-Kopp Treatment of the Heat Capacity of Stoichiometric Phases for Use in Computational Thermodynamics, *J. Phase Equil. Diffus.*, 2019, **40**, p 104–114.
69. J.M. Joubert, B. Kaplan, and M. Selleby, The Specific Heat of Al-based Compounds, Evaluation of the Neumann-Kopp rule and Proposal for a Modified Neumann-Kopp rule, *Calphad*, 2023, **81**, p 102562.
70. PANDAT Education 2025, Software for Multicomponent Phase Diagram Calculation by Computherm LLC, Middleton, WI 53562 USA. www.computherm.com.
71. Q. Chen and B. Sundman, Calculation of Debye Temperature for Crystalline Structures - A Case Study on Ti, Zr, and Hf, *Acta Mater.*, 2001, **49**(6), p 947–961.
72. Q. Chen and B. Sundman, Modeling of Thermodynamic Properties for Bcc, Fcc, Liquid, and Amorphous Iron, *J. Phase Equilib.*, 2001, **22**, p 631–644.
73. J. Ågren, Thermodynamics of Supercooled Liquids and Their Glass Transition, *Phys. Chem. Liq.*, 1988, **18**, p 123–139.
74. C.A. Becker, J. Ågren, M. Baricco, Q. Chen, S.A. Decterov, U.R. Kattner, J.H. Perepezko, G.R. Pottlacher, and M. Selleby, Thermodynamic Modelling of Liquids: CALPHAD Approaches and Contributions from Statistical Physics, *Phys. Status Solidi B*, 2014, **251**, p 33–52.
75. G. Grimvall, Thermophysical Properties of Materials, Elsevier Science B.V., 1999.
76. M. Forsblom, and G. Grimvall, Heat Capacity of Liquid Al: Molecular Dynamics Simulations, *Phys. Rev. B*, 2005, **72**, p 132204.
77. J. Hirschfelder, D. Stevenson, and H. Eyring, A Theory of Liquid Structure, *J. Chem. Phys.*, 1937, **5**, p 896–912.
78. Y. Sun, H. Muta, and Y. Ohishi, Heat Capacity of Liquid Transition Metals Obtained with Aerodynamic Levitation, *J. Chem. Thermodyn.*, 2022, **171**, p 106801.
79. P.F. Paradis, T. Ishikawa, and S. Yoda, Non-Contact Measurements of Thermophysical Properties of Niobium at High Temperature, *J. Mater. Sci.*, 2001, **36**, p 5125–5130.
80. S.V. Onufriev, V.A. Petukhov, V.R. Pesochin, and V.D. Tarasov, The Thermophysical Properties of Hafnium in the Temperature Range from 293 to 2000 K, *High Temp.*, 2008, **46**, p 203–211.
81. M.A. Tylkina, I.A. Tsyganova, and E.M. Savitskii, The Hafnium–Niobium System, *Russ. J. Inorg. Chem.*, 1964, **9**, p 893.
82. E. Rudy, Tech. Rep. No. AFML-TR-65-2, Part V. Air Force Materials Laboratory Research and Technology Division, Air Force Systems Command, Wright-Patterson Air Force Base, Ohio, 1969.
83. R.E. Siemens, H.R. Babitzke, H. Kato, US Bureau of Mines Report of Investigations, No. 6492, US Dept. of the Interior, Washington, 1964.
84. R.W. Carpenter, C.T. Liu, and P.G. Mardon, Phase Relations in Concentrated Ta-Hf and Nb-Hf Alloys, *Metallurg. Trans.*, 1971, **2**, p 125–131.
85. R.P. Elliott, Ph.D Thesis, Illinois Institute of Technology, Chicago, Illinois, 1955.
86. E.T. Hayes, D.K. Deardorff. U.S. At. Energy Comm. USBM-U-345, August 1957. Cited in D.K. Deardorff, O.N. Carlson, and H. Kato: "The Metallurgy of Hafnium," D.E. Thomas and E.T. Hayes, ed., U.S. At. Energy Comm., 1960. pp. 191-210.
87. D.P. Harmon, USAF Tech. Rept. AFML-TR-65-2, Part II, Vol. VI, August 1966 in E. Rudy, ed., Ternary Phase Equilibria in Transition Metal-Boron-Carbon-Silicon Systems. Part V., Compendium of Phase Diagram Data, Tech. Rep. AFML-TR-62-2, Air Force Materials Laboratory, Wright-Patterson Air Force Base, OH, 1969, p. 73.
88. R.F. Domagala, The zirconium-hafnium system, *J. Less Common Met.*, 1966, **11**(1), p 70–72.
89. E.F. Westrum Jr., Appendix III: Heat Capacity and Thermodynamic Properties from 5 to 350 K, Thermodynamics and Kinetic Studies for a Refractory Materials Program, Air Force Materials Laboratory, Research and Technology Division, Air Force System Command, Wright-Patterson Air Force Base, OH, L.A. McClaine (Ed.), Rept. ASD-TDR-62-204, Part III, April 1964, p. 189-196.
90. R. Hultgren, P.D. Desai, D.T. Hawkins, M. Gleiser, K.K. Kelley, and D.D. Wagman, *Selected Values of the Thermodynamic Properties of the Elements*. American Society for Metals, Metals Park, OH, 1973.
91. P.J. Spencer, Hafnium: Physico-Chemical Properties of It's Compounds and Alloys. I. Thermochemical Properties, Atomic Energy Review Special Issue No 8, K.L. Komarek, Ed., International Atomic Energy Agency, Vienna, 1981, p. 9-53
92. L.V. Gurvich, I.V. Veits, V.A. Medvedev, G.A. Bergman, V.S. Yungman, G.A. Khachkuruzov, V.S. Yorish, O.V. Dorofeeva, E.L. Osina, P.I. Tolmach, I.N. Przheval'skii, I. Nazarenko, N.M. Aristova, E.A. Shenyavskaya, L.N. Gorokhov, A.L. Rogatskii, M.E. Emifov, V.Y. Leonidov, Y.G. Khait, A.G. Efimova, S.E. Tomberg, A.V.Gusarov, N.E. Khandamirova, G.N. Yurkov, L.R. Fokin, L.F. Kuratova, and A.D. Gol'dshtein. in V.P. Glushko, L.V. Gurvich, G.A. Bergman, I.V. Veits, V.A. Medvedev, G.A. Khachkuruzov, V.S. Yungman (Ed), Termodinamicheskie Svoistva Individual'nykh Veshchestv, Nauka, Moscow, 1982
93. M.W. Chase, NIST-JANAF Thermochemical Tables, *J. Phys. Chem. Ref. data*, 1998, **28**, p 1951.
94. I. Barin and G. Platzki, *Thermochemical data of pure substances*. VCh, Weinheim, 1989.
95. M.M. Martynyuk and V.I. Tsapkov, The Resistivity, Enthalpy and Phase Transitions of Titanium, Zirconium and Hafnium during Pulse Heating, *Izv. Akad. Nauk SSSR, Met.*, 1974, **2**, p 181–185.
96. R.J. Ackermann and E.G. Rauh, The Thermodynamics and Vaporization of Thorium, Hafnium and Zirconium, *J. Chem. Thermodyn.*, 1972, **4**, p 521–532.

97. J.P. Abriata and D.E. Laughlin, The Third Law of Thermodynamics and Low Temperature Phase Stability, *Prog. Mater. Sci.*, 2004, **49**(3–4), p 367–387.
98. P.P. Fedorov, Third Law of Thermodynamics as Applied to Phase Diagram, *Russ. J. Inorg. Chem.*, 2010, **35**, p 1722–1739.
99. D.E. Laughlin and W.A. Soffa, The Third Law of Thermodynamics: Phase Equilibria and Phase Diagrams at Low Temperatures, *Acta Mater.*, 2018, **145**, p 49–61.
100. D.E. Laughlin and T.B. Massalski, Construction of Equilibrium Phase Diagrams: Some Errors to be Avoided, *Prog. Mater. Sci.*, 2021, **120**, p 100715.
101. U. Pinsook and G.J. Ackland, Calculation of Anomalous Phonons and the hcp-bcc Phase Transition in Zirconium, *Phys. Rev. B Cond. Matter Mater. Phys.*, 1999, **59**(21), p 13642–13649.
102. D. Srivastava, S. Banerjee, and S. Ranganathan, The Crystallography of BCC to HCP Martensitic Transformation in Dilute Zr-Nb alloys: Part II: Application of Phenomenological Theory of Martensitic Transformation, *Trans. Indian Inst. Met.*, 2004, **57**(5), p 427–449.
103. A. Taylor and N.J. Doyle, The Constitution Diagram of the Niobium-Hafnium System, *J. Less-Common Met.*, 1964, **7**, p 34–53.
104. B.J. Wendell, R. Taggart, and D.H. Polonis, Beta Decomposition Processes in Hf-Rich Hf-Nb Alloys, *Metall. Trans. A*, 1978, **9A**, p 723–729.
105. G.M. Benites, A. Fernández Guillermet, G.J. Cuello, and J. Campo, Structural Properties of Metastable Phases in Zr-Nb Alloys I. Neutron Diffraction Study and Analysis of Lattice Parameters, *J. Alloys Compd.*, 2000, **299**, p 183–188.